Chapter 4
OBSERVATION RESULTS AND ANALYSIS OF DATA

4.1 INTRODUCTION

Eight specimens, four parallel and four perpendicular to the direction of maximum applied compressive stresses, were extracted from each experiment as described in Chapter 2. For purposes of analysis, only the specimens parallel to the direction of the maximum compression, i.e. specimens 1, 2, 3, and 4 in Figure 2.25, were examined. A minimum of 55 scanning electron microscope (SEM) images were taken from each specimen, bringing the total number of analyzed images to over 2,220.

Computer programs were developed to analyze the images. These were based both on the concept of stereology as described in Chapter 3, and also on two-dimensional measurements (such as the number of cracks per unit of observed area, crack lengths, and crack orientation) for every image. The computer programs are outlined in Appendix B. The analysis was performed using an image analyzer with the commercial name, Kontron Image Analyzer. The quantitative and qualitative analysis of the data obtained from the image analysis is presented in this chapter.

4.2 CHARACTERIZATION OF MICROCRACK INITIATION

The characterization of the microcrack initiation was studied under the scanning electron microscope (SEM) and on micrographs of cross sections of the specimens for different conditions of confining stresses.

No stress-induced microcracks were observed in the reference specimen, which was subjected to only a small compressive stress when filled with molten metal at a pressure of 1,500 psi (10.3 MPa). Figure 4.1 shows two micrographs from the no-load experiment.

It is important to note that concrete is inherently cracked even before the application of any load (Hsu et al. 1963). Existing pre-load cracks are due to factors such as bleeding, creep, drying shrinkage, etc.

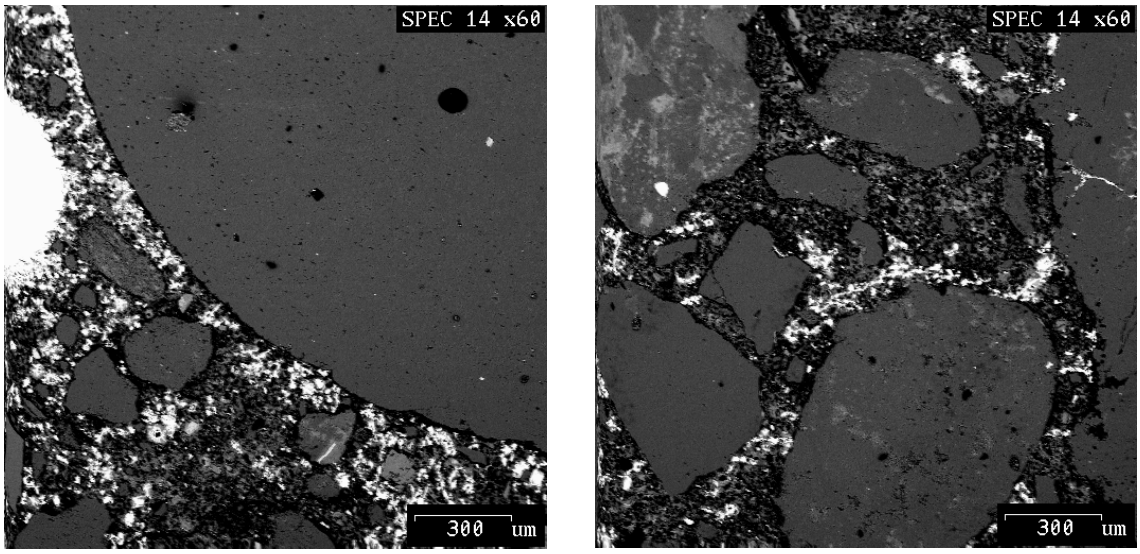

Figure 4.1 SEM micrographs from the no-load experiment

The microcracks in the rest of the specimens appear to have been generated by several different mechanisms. Figure 4.2 shows two micrographs taken from a specimen under confining condition #3; that is, uniaxial compression in the central portion, with ends constrained by pre-tensioned wire, and a pore pressure of 1,500 psi (10.3 MPa). As can be seen, microcracks propagate through the cement paste and along the transition zone.

Many cracks were generated from voids in a mechanism similar to that suggested for rocks by Lajtai (1974), Olson (1974), and Sammis and Ashby (1986). Figure 4.3 shows two micrographs of microcracks generated from a pore space, which is filled with Wood's metal. These microcracks were generated as a result of local tensile stress tangential to the boundary of voids, with a value that was of the order of the maximum applied principal stress. It was found that these cracks usually start from the pore boundaries and then propagate in the direction of maximum compression.

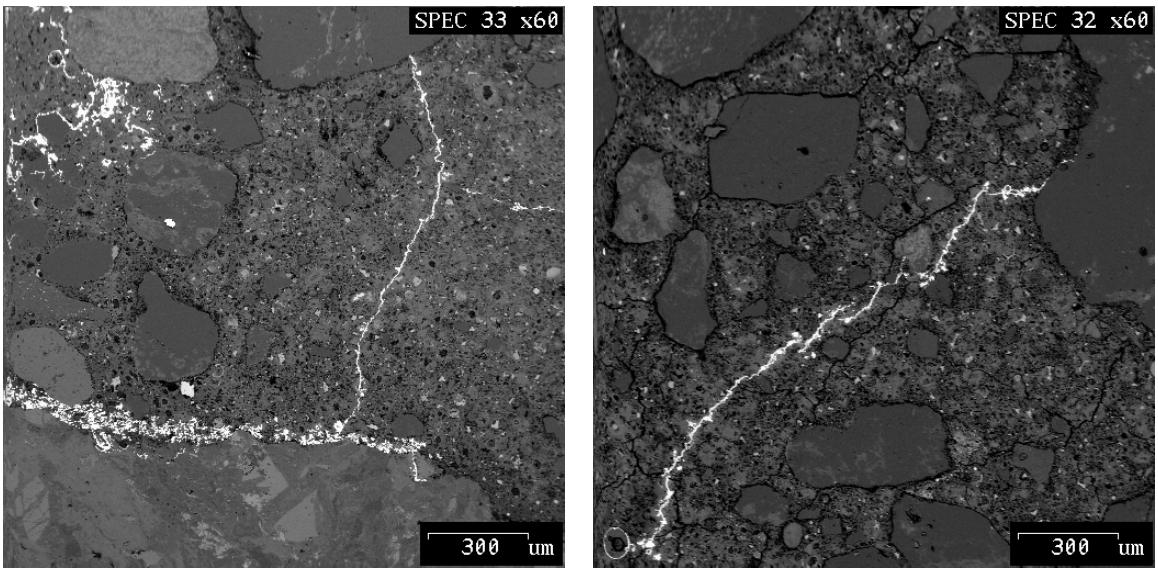

Figure 4.2 SEM micrographs from the partially confined experiment

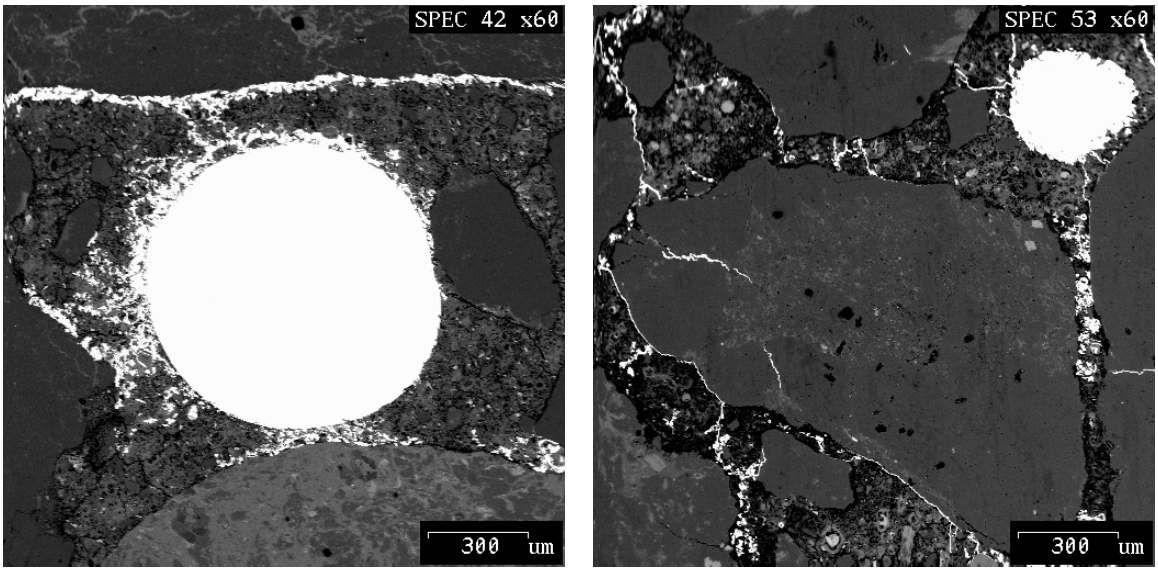

Figure 4.3 SEM micrographs of microcracks propagating from a pore

Microcracks were also found to have been generated from the inside of aggregates, in a manner similar to a Brazilian test, when the aggregates were loaded across their height. Figure 4.4 shows four micrographs of this phenomenon for three different loading conditions- fully confined, partially confined, and uniaxial.

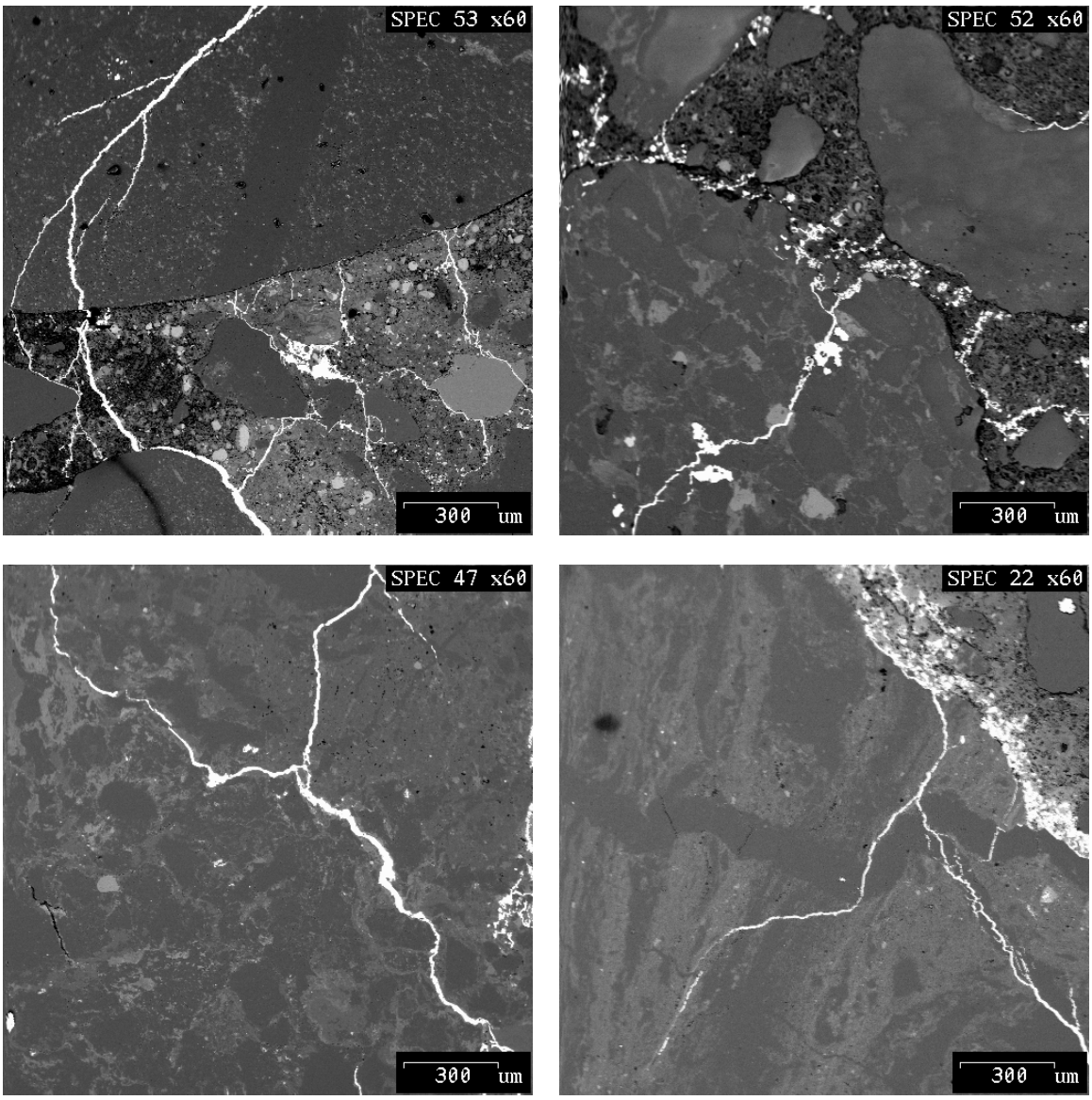

Figure 4.4 SEM micrographs of aggregate cracking

High-strength concrete behaves more like a homogeneous material than does normal-strength concrete. The stress-strain curves for high-stress concrete are steeper and closer to linearity to a high stress-strength ratio than in normal-strength concretes. This is because of a decrease in the amount and extent of microcracking in the transition zone. Thus the high-strength concrete exhibits a more brittle mode of fracture and less volumetric dilation (Carrasquillo et al. 1981). High-strength concrete has a stronger and tougher cement paste due to a

lower water/cement ratio, which results in a closer packing of cement grains and a reduced amount of pores and cracks. Apart from this microstructurally improved matrix, high-strength concrete also has a stronger transition zone- the area of interface between the cement matrix and the aggregates. This presumably results from the reduction of excess bleeding and the filling of gaps by admixtures, which in this case was rice husk ash. The microstructural differences between high-strength and normal-strength concrete cause significant differences in their deformation and fracture behavior. For example, high-strength concrete tends to behave with greater linear elasticity up to its peak strength, while normal-strength concrete typically exhibits non-linear behavior, possibly because of interfacial crack extension prior to peak strength (Carrasquillo et al. 1981; Huang et al. 1989; ACI Committee 363, 1984). Further, fracture development in high-strength concrete is usually accompanied by a relatively small process zone and tends to be characterized better by linear elastic fracture mechanics than does to normal-strength concrete (Gettu et al. 1990).

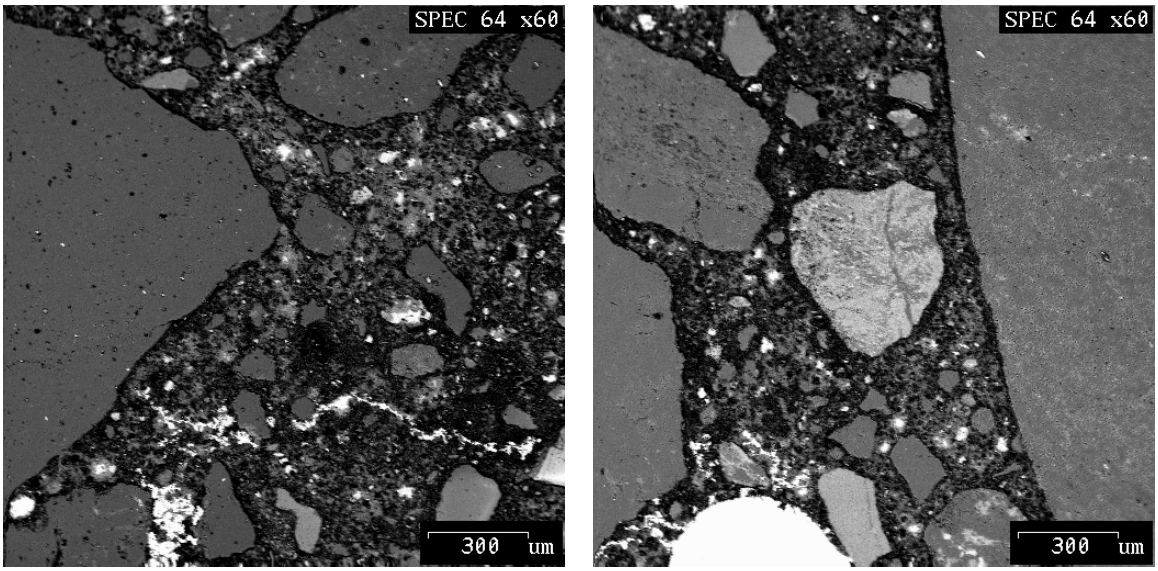

Figure 4.5 SEM micrographs from the no-load experiment for high-strength concrete specimen

Figure 4.5 shows two SEM micrographs from the reference specimen of high-strength concrete, which is a no-load sample. No stress-induced microcracks were observed in the reference specimens. The microcracks observed in these micrographs are attributed to factors such as drying shrinkage.

Figure 4.6 shows four SEM micrographs of a high-strength concrete specimen from Experiment #7, which was conducted under uniaxial loading condition- that is, uniaxial compression with no confinement and a pore pressure of 1,500 psi (10.3 MPa).

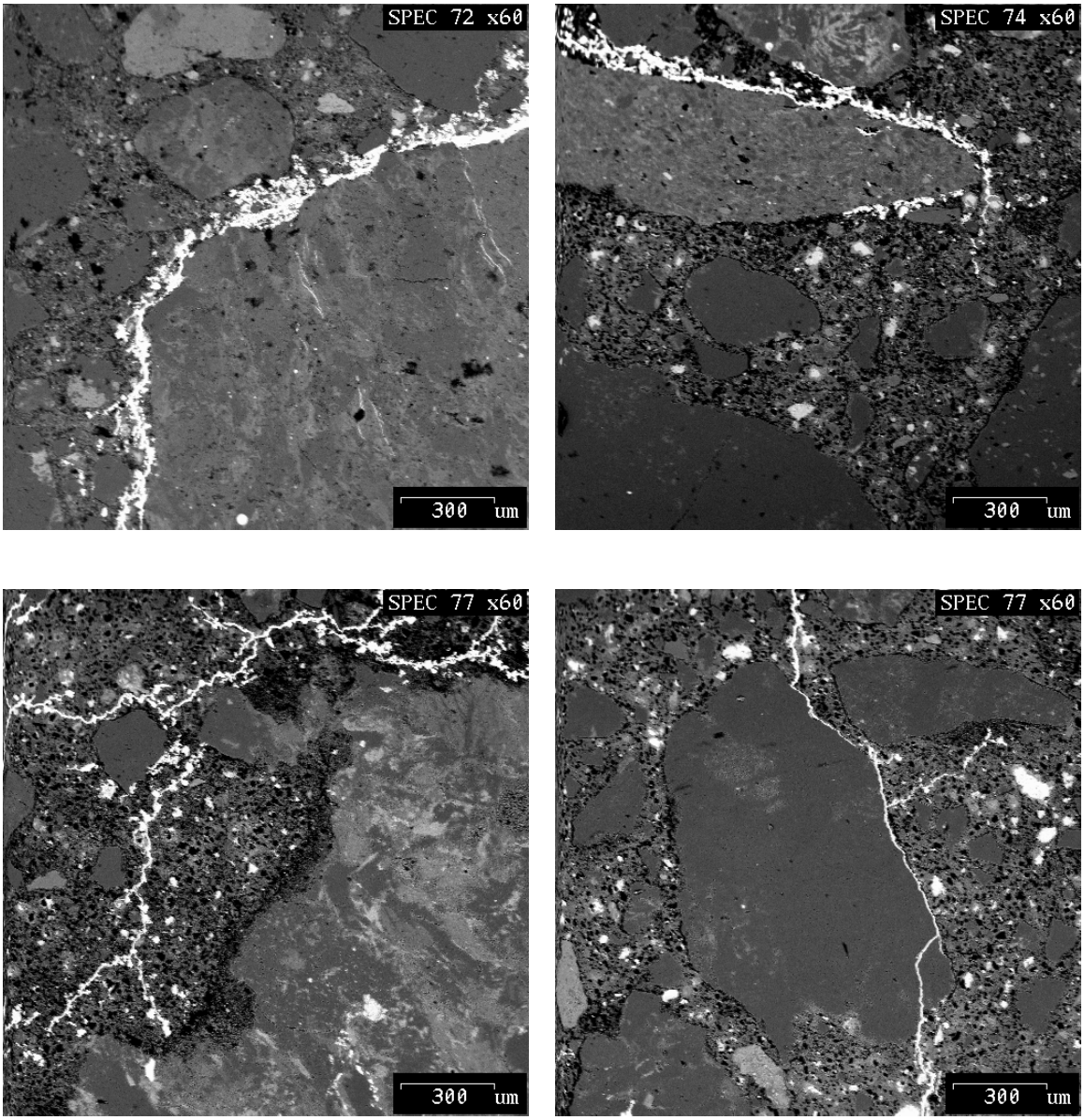

Figure 4.6 SEM micrographs from the partially confined experiment for high-strength concrete

It is clear, then, that less cracking occurs in high-strength than in normal-strength concrete; and because of the stronger cement paste, most of this cracking takes place in the transition zone.

4.3 ORIENTATION OF MICROCRACKS

Most of the microcracks observed were subparallel to the direction of the maximum compression. In all the specimens on which the observations were made, the microcracks were found to exist within a few degrees of the direction of the maximum compression. Figures 4.7 and 4.8 show the microcrack orientation for normal and high-strength concrete specimens. Confined 1 and confined 2 refer to experiments 3 and 4 respectively (see Appendix A). The degree of orientation obtained for the partially confined specimens were base on the cracks in the confined portion.

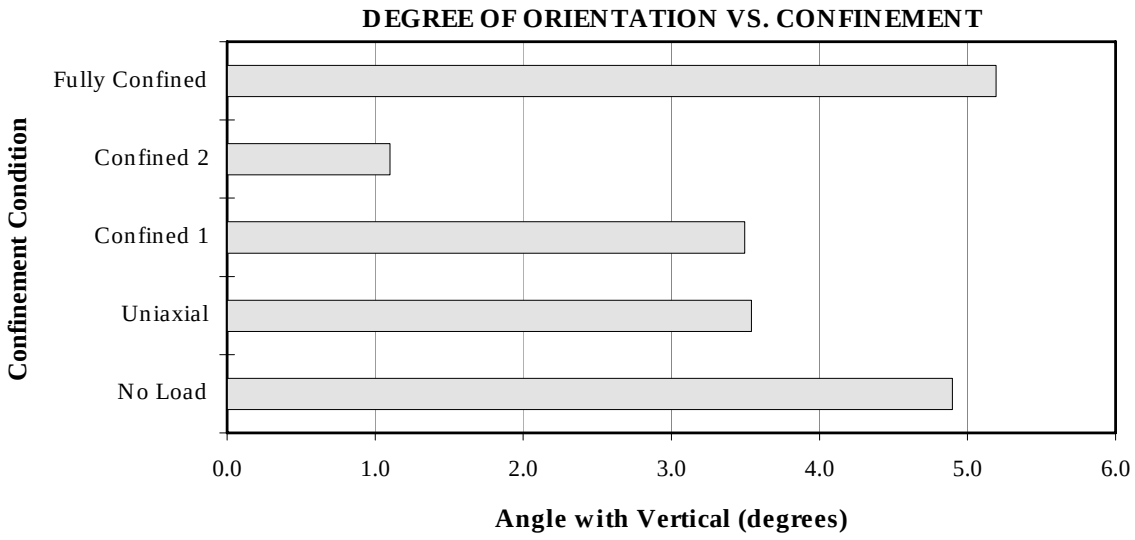

Figure 4.7 Average crack orientation for normal-strength concrete (results of confined 1 and 2 conditions are from the confined portion of the specimen)

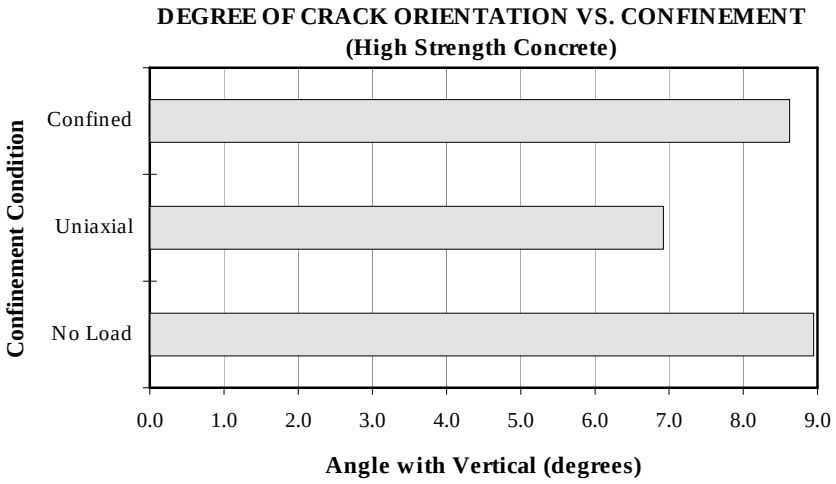

Figure 4.8 Average crack orientation for high-strength concrete

The orientation of microcracks in these figures were algebraic averages of the orientation of the microcracks within each 512×512 pixel square on the corresponding SEM images. The average orientation of microcracks in each of the specimens are listed in Table 4.1. The average values and standard deviations of the orientations listed in the table were obtained assuming normal distribution and using absolute values (ignoring signs) of the angle from the planes of the microcracks to the direction of the maximum compression. The overall average value and standard deviation of the orientation from the normal-strength concrete specimens were 5 degrees and 3 degrees, respectively. The same average values for high-strength concrete were 8 degrees and 2 degrees, respectively.

Table 4.1 Number, length, and orientation of microcracks

		Unsmoothed Crack			Smoothed Crack		
CONC. TYPE	EXPERIMENT TYPE	AVE. NO. OF CRACKS	AVE. LENGTH OF CRACKS	AVE. ANGLE WITH VERTICAL	AVE. NO. OF CRACKS	AVE. LENGTH OF CRACKS	AVE. ANGLE WITH VERTICAL
Normal Strength Concrete	No Load	60	51.4	4.9	21	81.7	2.9
	Uniaxial	86	51.8	3.5	29	85.4	3.3
	Confined 1	65	50.5	3.5	21	80.0	0.8
	Confined 2	37	50.6	1.1	12	73.4	5.9
	Fully Confined	35	49.5	5.2	16	74.8	2.4
High Strength Concrete	No Load	56	39	8.9	20	56.4	2.7
	Uniaxial	82	45	6.9	31	74.0	2.1
	Confined	53	39	8.6	19	51.0	2.9

Table 4.2 summarizes the results of stereological analysis. As described in Chapter 3, after a binary image of the crack network is developed, that binary image is then intersected by an array of straight parallel lines at angles of 0°, 15°, 30°, 45°, 60°, 75°, 90°, 105°, 120°, 135°, 150°, and 165°. The number of crack intercepts at a given angle is measured according to the number of intersections on line array at that angle with the crack network in the binary image.

$$\text{Number of Crack Intercepts}(\theta) = \text{FIELDCOUNT}$$

Table 4.2 also shows the total area of the cracks in the binary image. Since the area of each image is known, the percent of the area that is cracked (i.e., crack density) can be determined. Another value in the table below is the surface-to-volume ratio, S_V, determined from the basic equation for obtaining the area of surfaces in a volume, $S_V = 2P_L$. The last column in the table shows the number of crack nodes, which indicates crack branching. For each parameter two values are measured: the first one relates to the unsmoothed crack network from the binary image, and the second value relates to the smoothed version of the cracks.

Table 4.2 Data from stereological analysis

Unsmoothed Crack																		
SPECIMEN	AREA	% AREA	0	15	30	45	60	75	90	105	120	135	150	165	180	TOTAL	S_v	NODES
No Load	8223	1.00	31	31	29	27	29	31	30	30	28	25	28	32	31	349	1.1E-3	28
Uniaxial	11843	1.53	47	48	44	39	41	42	41	42	39	36	42	47	47	506	1.6E-3	40
Confined 1	7337	0.86	28	28	26	24	25	27	27	27	25	22	25	27	28	311	9.6E-4	26
Confined 2	7005	0.77	26	26	25	23	25	27	26	26	24	22	24	26	26	299	9.3E-4	24
Fully Confined	6485	0.74	25	24	23	20	22	23	22	23	21	20	22	25	25	269	8.3E-4	25
No Load	5228	0.98	21	20	19	16	18	20	19	19	18	16	18	20	21	226	7.0E-4	18
Uniaxial	10829	1.90	43	43	39	35	38	41	39	40	36	34	39	43	43	470	1.5E-3	32
Confined	6274	1.21	25	25	23	20	22	23	22	22	21	19	23	25	25	269	8.3E-4	21
Smoothed Crack																		
SPECIMEN			0	15	30	45	60	75	90	105	120	135	150	165	180	TOTAL	S_v	NODES
NO LOAD			20	19	18	15	18	20	21	20	17	15	17	19	20	227	0.00070	4
UNIAXIAL			30	31	27	25	28	30	31	30	26	23	26	30	30	350	0.00108	8
CONFINED 1			18	17	16	14	16	18	19	18	16	13	16	17	18	205	0.00063	4
CONFINED 2			18	18	16	14	17	18	19	18	16	14	15	17	18	206	0.00064	4
FULLY CONFINED			15	14	13	11	12	14	14	14	12	11	13	14	15	166	0.00052	3
NO LOAD			14	14	12	10	12	13	14	13	12	10	12	14	14	155	0.00048	3
UNIAXIAL			31	31	27	25	27	30	31	30	27	23	27	30	31	348	0.00108	7
CONFINED			17	16	14	12	14	15	16	15	14	11	14	16	17	181	0.00056	3

Figures 4.9 and 4.10 are the plots of the number of intercepts of line arrays with the crack networks.

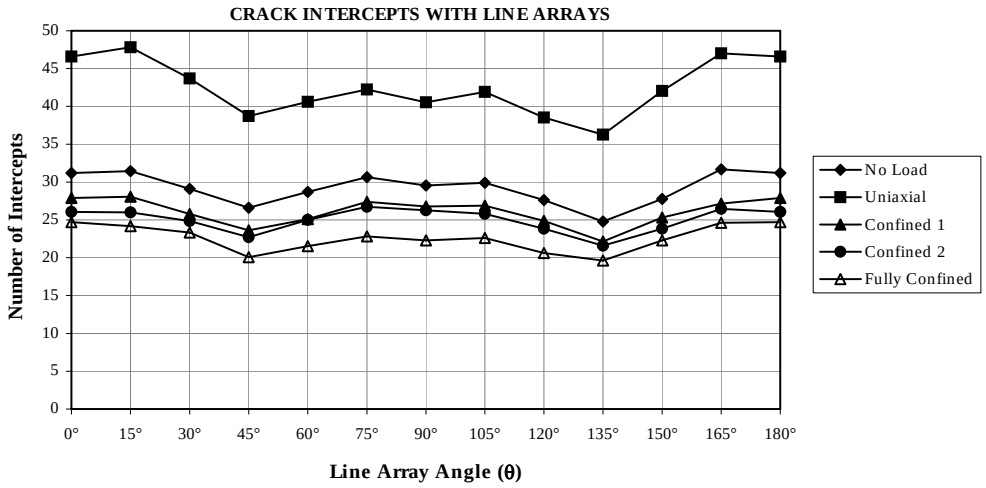

Figure 4.9 Crack orientation for normal-strength concrete

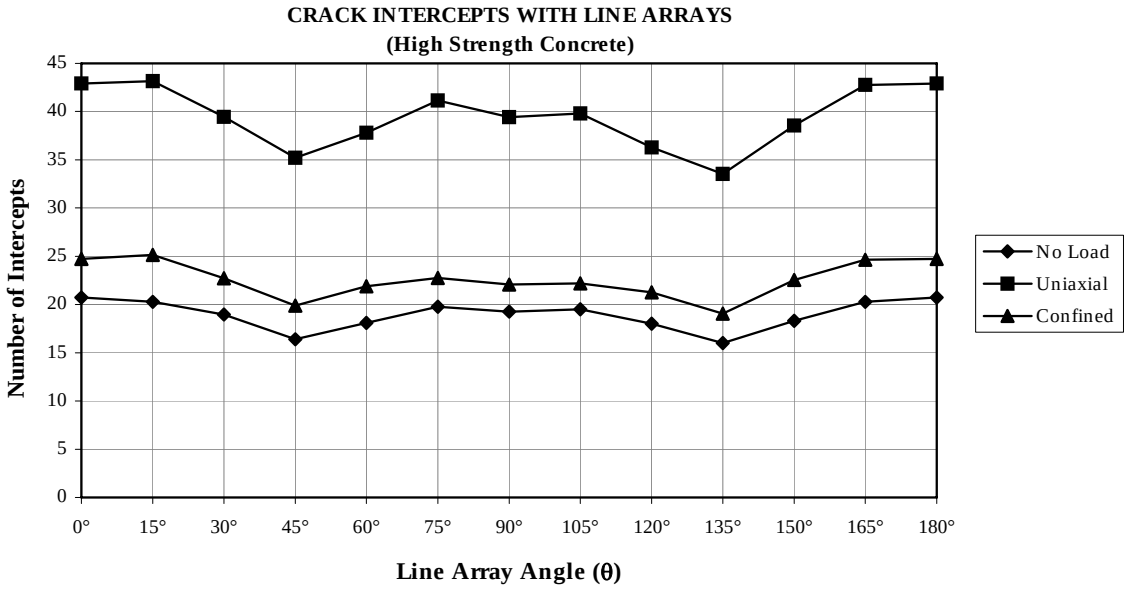

Figure 4.10 Crack orientation for high-strength concrete

Figures 4.11 and 4.12 are the plots of numbers of intercepts of line arrays with the smoothed crack networks.

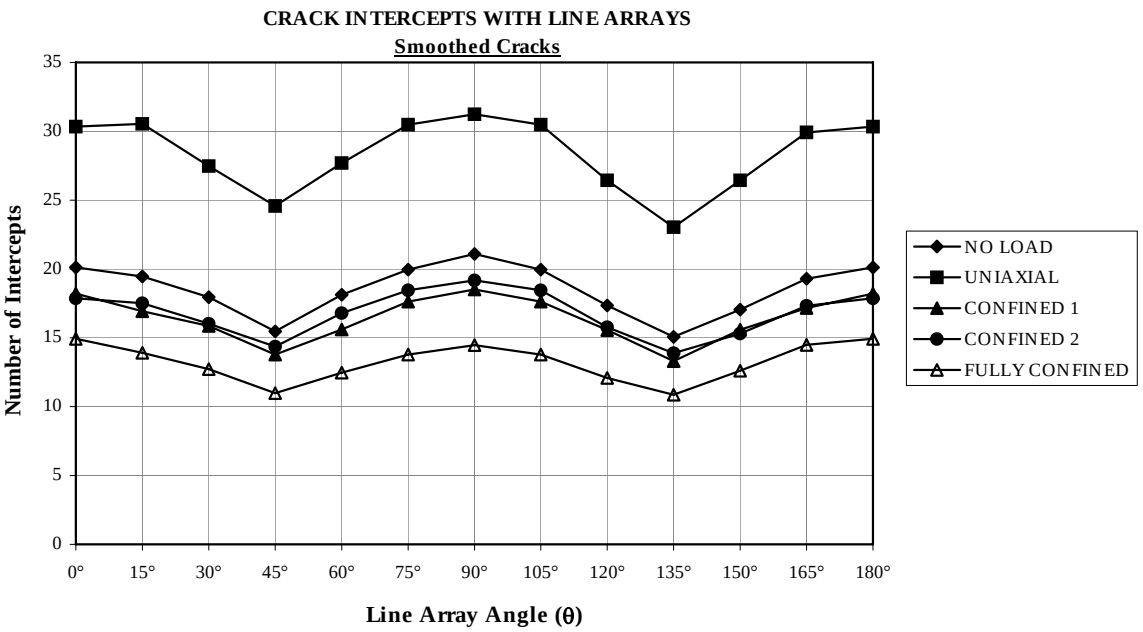

Figure 4.11 Number of intercepts for smoothed cracks

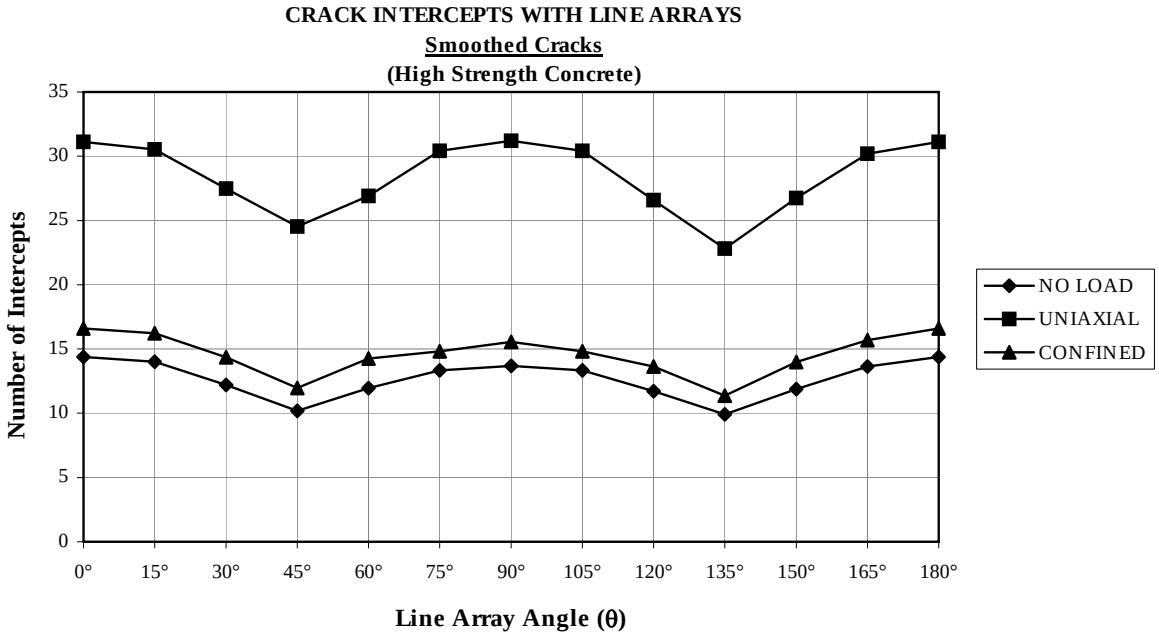

Figure 4.12 Number of intercepts for smoothed cracks

Another way to determine the anisometry of the crack network, $P_L(\theta)$, is to plot it in a polar figure according to the specific orientation of the cracks. The plot of number of intersections versus orientation (in 12 equal angle steps) covers only the range of 0-180 degrees (the range 180-360 degrees is redundant), and is shown in different format than most distribution plots because the *compass rose* pattern makes it easier to interpret the data. A so-called *rose of the number of intersections* is constructed in this way. Figures 4.13 and 4.14 show the rose of the number of intersections for normal and high-strength concrete samples.

From Figures 4.9 through 4.14, it is evident that there is a definite orientation in the crack pattern, and that many cracks lie within 15 degrees of the direction of the maximum compression (between 0 to 15 degrees and 165 to 180 degrees). This holds true on all five normal-strength concrete specimens as well as the three high-strength specimens.

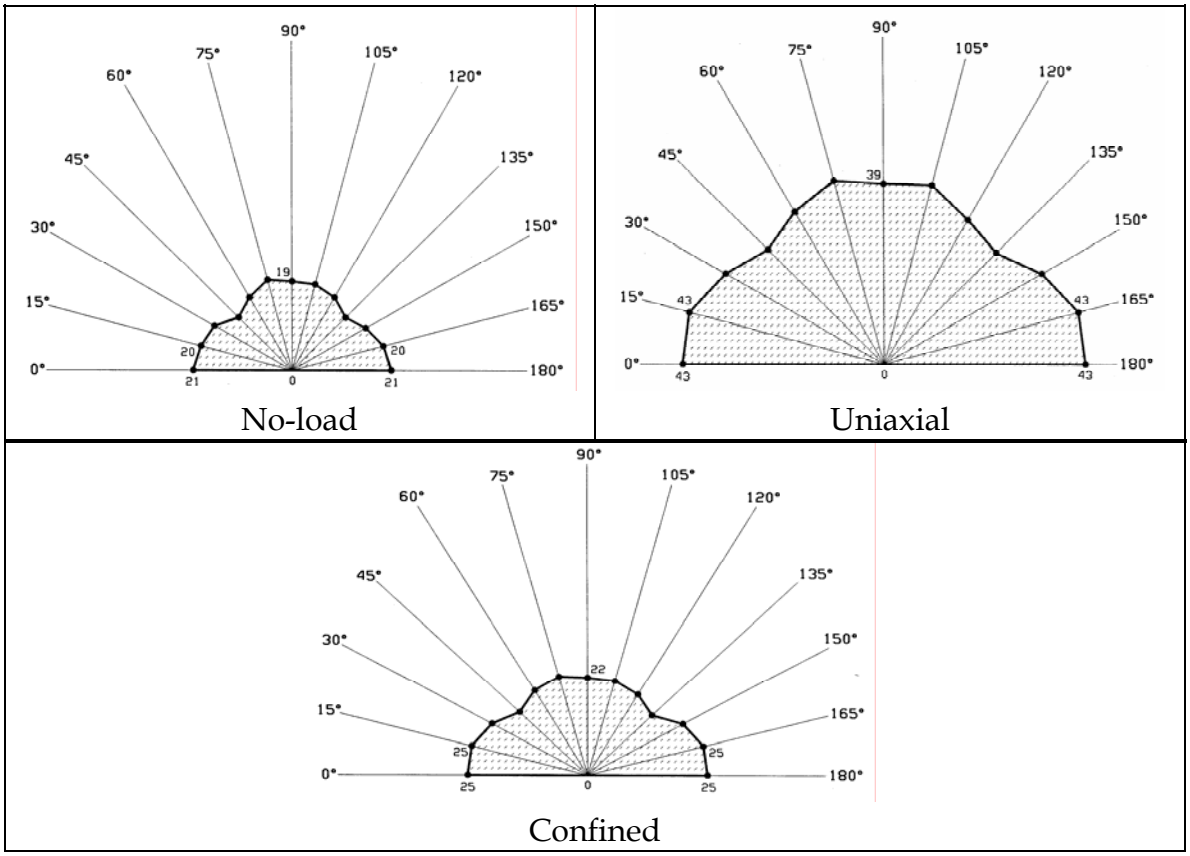

Figure 4.13 Rose of the number of intersections diagrams for high-strength concrete

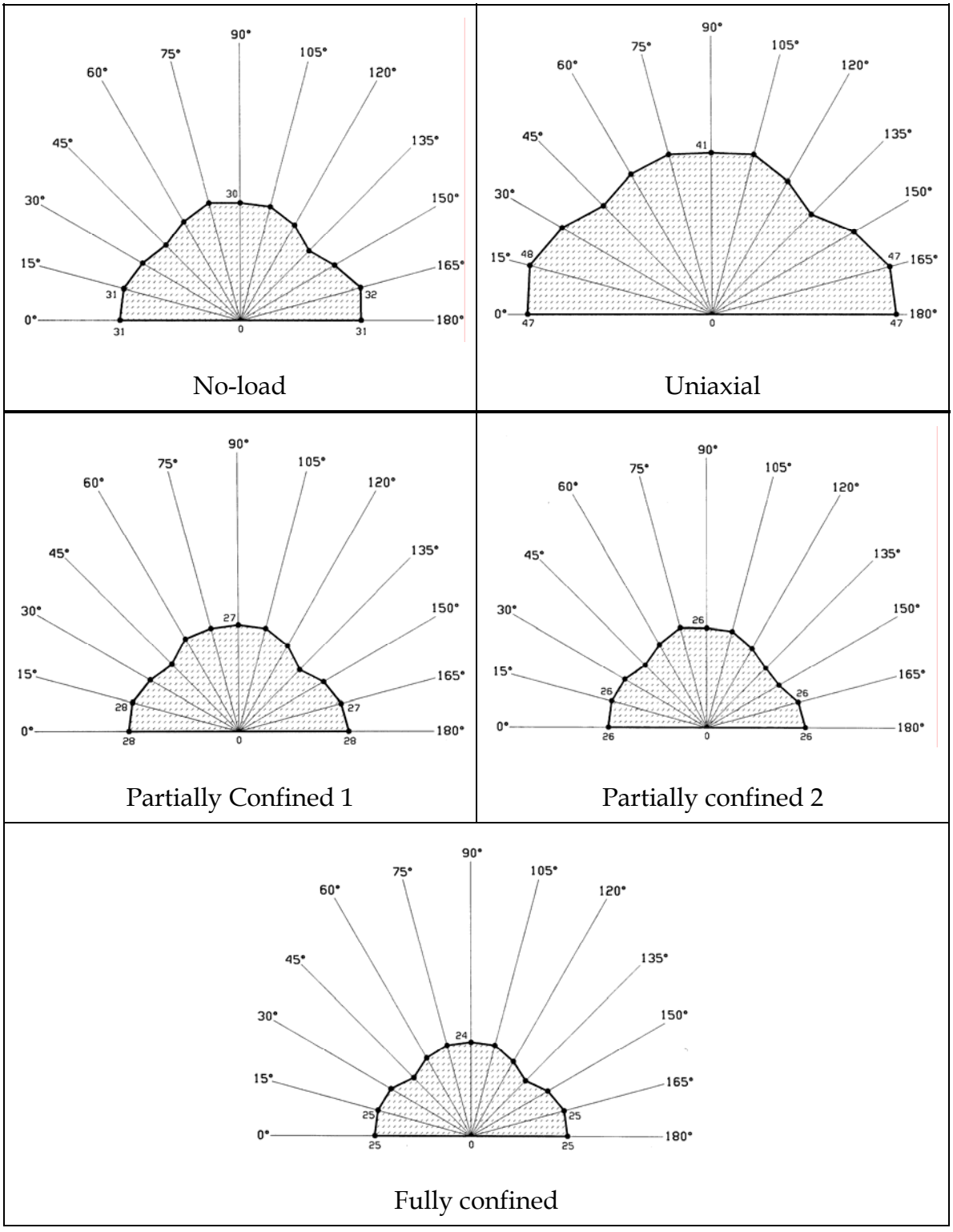

Figure 4.14 Rose of the number of intersections diagrams for normal-strength concrete

Careful examination of the micrographs reveal that microcracks may not necessarily be generated subparallel to the direction of the maximum compression. The initial orientation of the microcracks is dependent on the orientation of the local tensile stress which is responsible for the generation of the cracks (Zheng 1989). The microcracks turn towards the direction of maximum compression after they are generated and propagate in this direction throughout most of their length. The stress intensity factors generated by the overall stress field are favorable to opening microcracks against the least compressive stress. As a result, the microcracks turn towards the most favorable direction, which is parallel to the maximum compression.

Microcrack tips observed at a higher magnification appear to turn and change direction before they fully stop propagating. Figures 4.15 (a) and 4.15 (b) are higher magnification micrographs of crack tips that show this behavior.

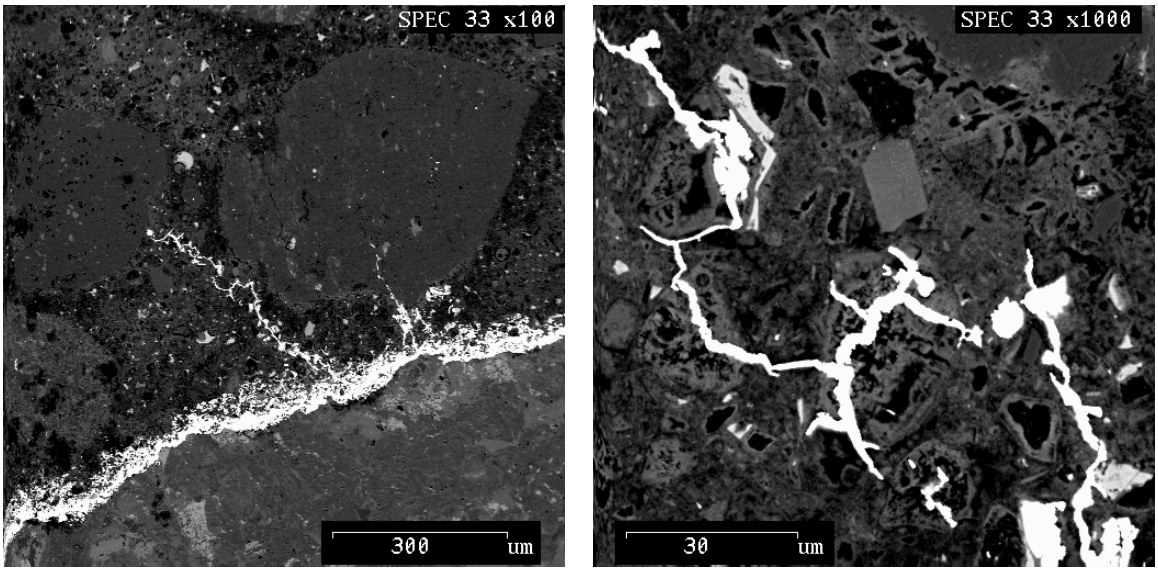

Figure 4.15 (a) SEM micrographs showing crack tips at higher magnification

(The direction of maximum compression is vertical)

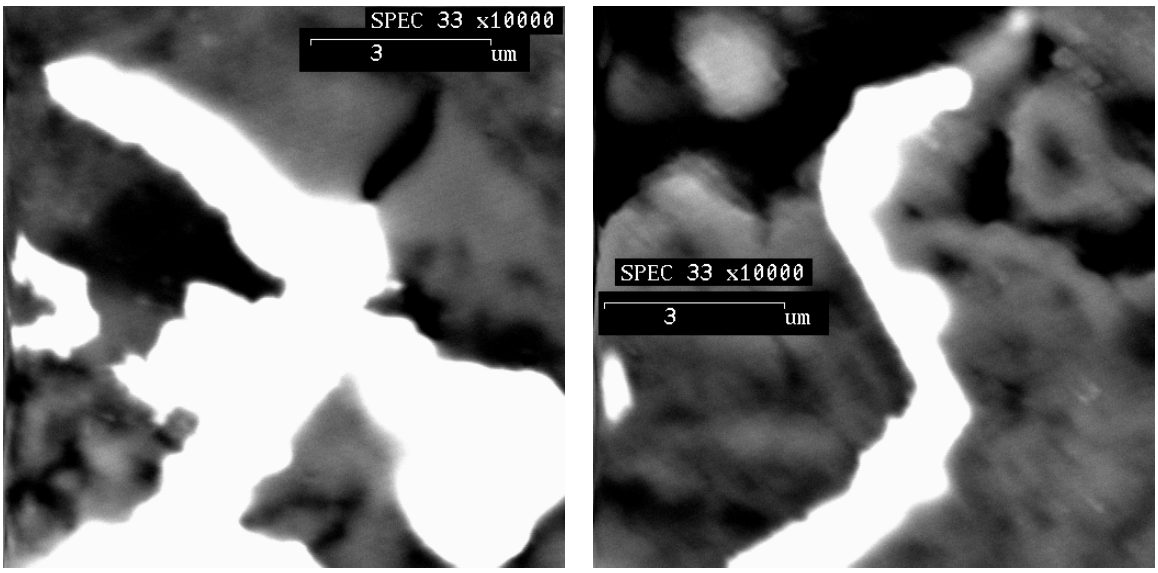

Figure 4.15 (b) SEM micrographs showing crack tips at higher magnification (The direction of maximum compression is vertical)

This phenomenon may be explained as follows. As the crack starts to propagate, the energy that causes the propagation of the cracks is much greater than the energy required to generate fresh new surfaces. At this stage, the direction of the crack propagation is mainly controlled by the direction of the stress intensity factor, which is usually greatest when the crack plane is perpendicular to the least compressive stress. The crack at this stage propagates in the direction of the maximum compression. By the end of propagation, the energy that drives it is insufficient to continue the crack along unfavorable surfaces, but is still greater than that required to open new surfaces along one of the weak planes. The crack then turns into the weak plane that had the smallest angle with the maximum compression (Zheng 1989).

4.4 MICROCRACK DENSITY DISTRIBUTION

The microcrack density distribution, Γ, represents the number of microcracks per unit of observation area. Pore spaces were not counted as microcracks. For a body of volume V (unit thickness) containing N cracks with initial cracks of length ℓ_0, the initial crack density parameter Γ is given by:

$$\Gamma = \frac{N\ell_0^2}{V} \tag{4.1}$$

The crack density parameter Γ, in an image of area A with N cracks of length ℓ_i, can be obtained from the following relationship:

$$\Gamma = \frac{\sum_{i=1}^{N} \ell_i^2}{A} \tag{4.2}$$

Where:

Γ = Crack density parameter

ℓ_i = Crack length (mm)

A = SEM image area (512 pixels × 512 pixels = 2.8358 mm^2)

Table 4.3 shows the average crack density parameters for all experiments. The reference specimen (no-load sample) has a relatively high crack density due to the fact that concrete is heavily cracked even before applying any load (Hsu et al. 1963). Hence, the effective crack density increase for the specimen subjected to applied loads is the difference between the final crack density and the crack density of the no-load specimen. The crack densities for the partially confined concrete cylinders in Table 4.3 are only the crack densities in the confined portion of the samples, i.e., specimens 1 and 2 in Figure 2.25. The tension in the wire wound around partially confined 2 sample (Experiment #4) is higher than that on partially confined 1 sample (Experiment #3).

Table 4.3 Crack density for different loading conditions

EXPERIMENT	CONCRETE TYPE	CRACK DENSITY
No-load	Normal-Strength	0.0444
Uniaxial	Normal-Strength	0.0919
Partially Confined 1	Normal-Strength	0.0308
Partially Confined 2	Normal-Strength	0.0285
Fully Confined	Normal-Strength	0.0262
No-load	High-Strength	0.0124
Uniaxial	High-Strength	0.1245
Partially Confined	High-Strength	0.0410

Figures 4.16 and 4.17 show the crack density as a function of confinement for normal and high-strength concrete specimens. From these two figures the effect of confinement on crack density is quite evident.

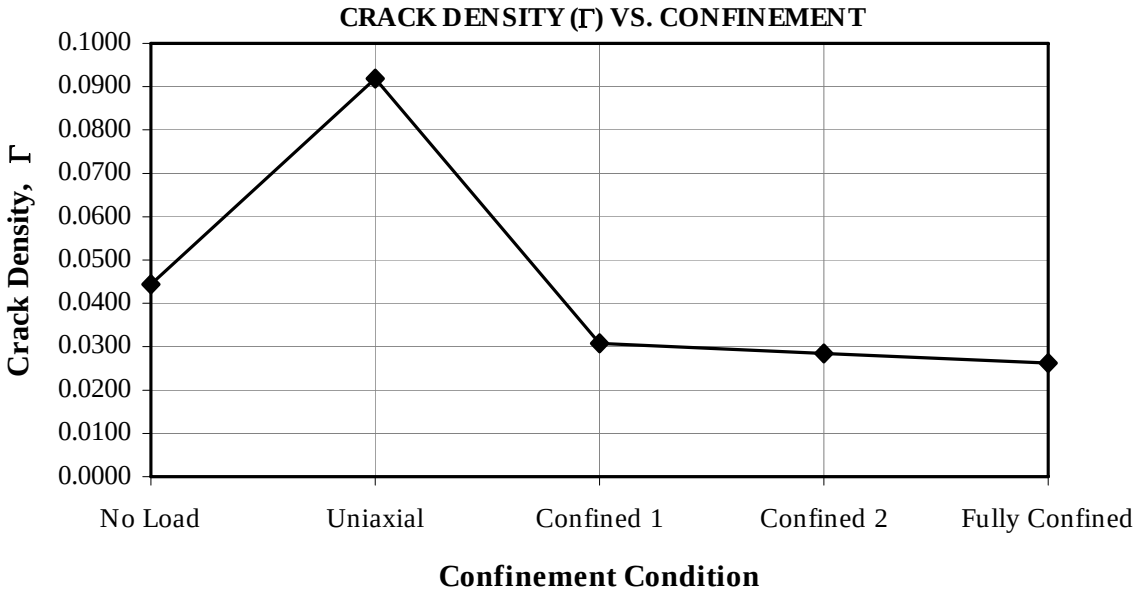

Figure 4.16 Crack density, Γ, as a function of confinement for normal-strength concrete

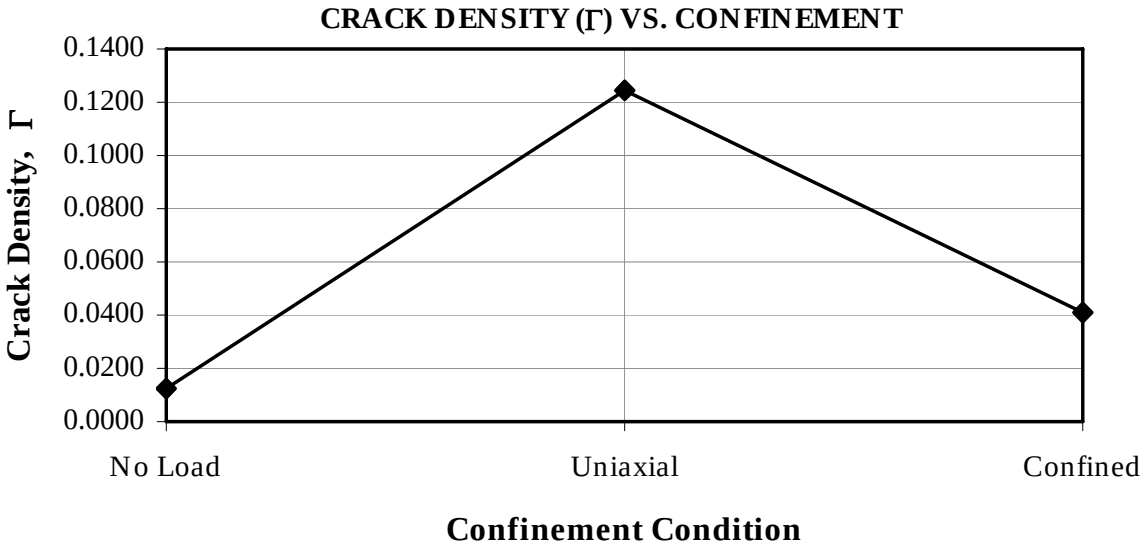

Figure 4.17 Crack density, Γ, as a function of confinement for high-strength concrete

The specimens subjected to uniaxial compression had the highest crack density. With increasing confining stress, the average crack densities decreased. Specimen 5, which was fully confined and subjected to the greatest confining stress, had the lowest crack density. Specimens 3 and 4 which were both partially confined, had very close crack densities. In the case of high-strength concrete, the number of cracks decreased substantially when confinement was introduced.

Figures 4.18 and 4.19 illustrate the crack length and crack densities for the partially confined specimens in both confined and unconfined portions of the specimen for Experiments #3 and #4 which were subjected to a confining stress over each end, and uniaxial compression over the center. In both cases the crack densities in the center and edge of the sample are smaller in the confined portion than in unconfined portion. Also, in both experiments, the average crack length is smaller in the center portion of the specimen than along the edge.

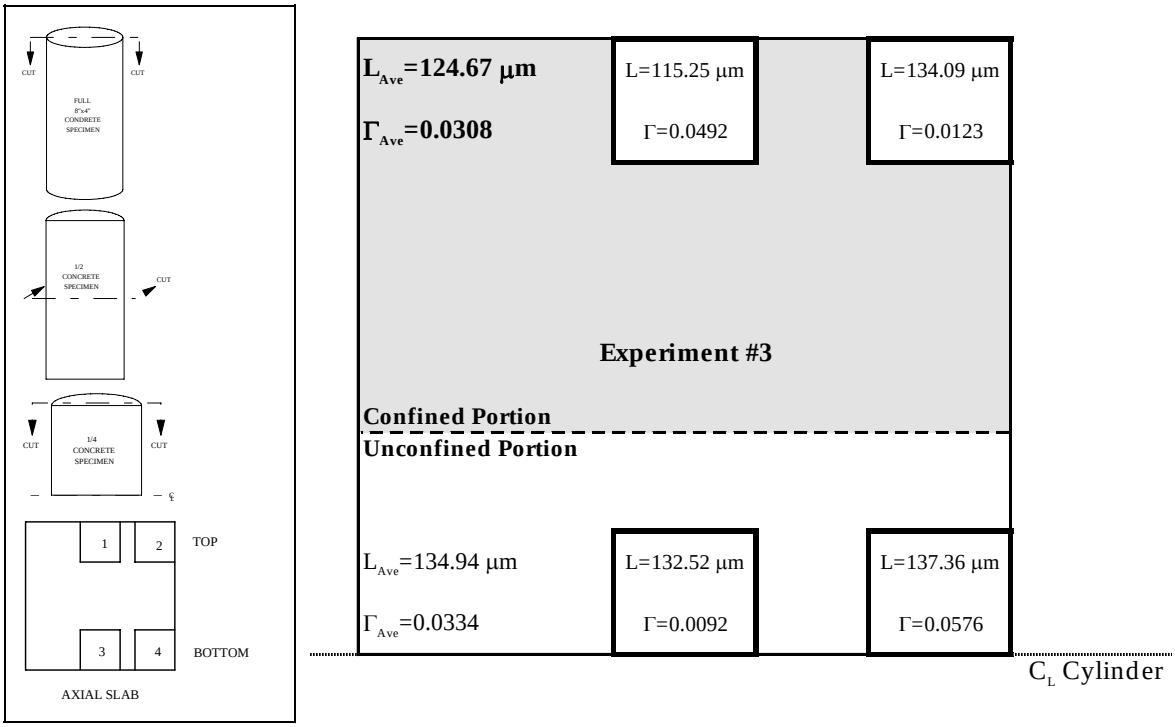

Figure 4.18 Diagrammatic representation of crack length and crack density at confined and unconfined portions of Experiment #3

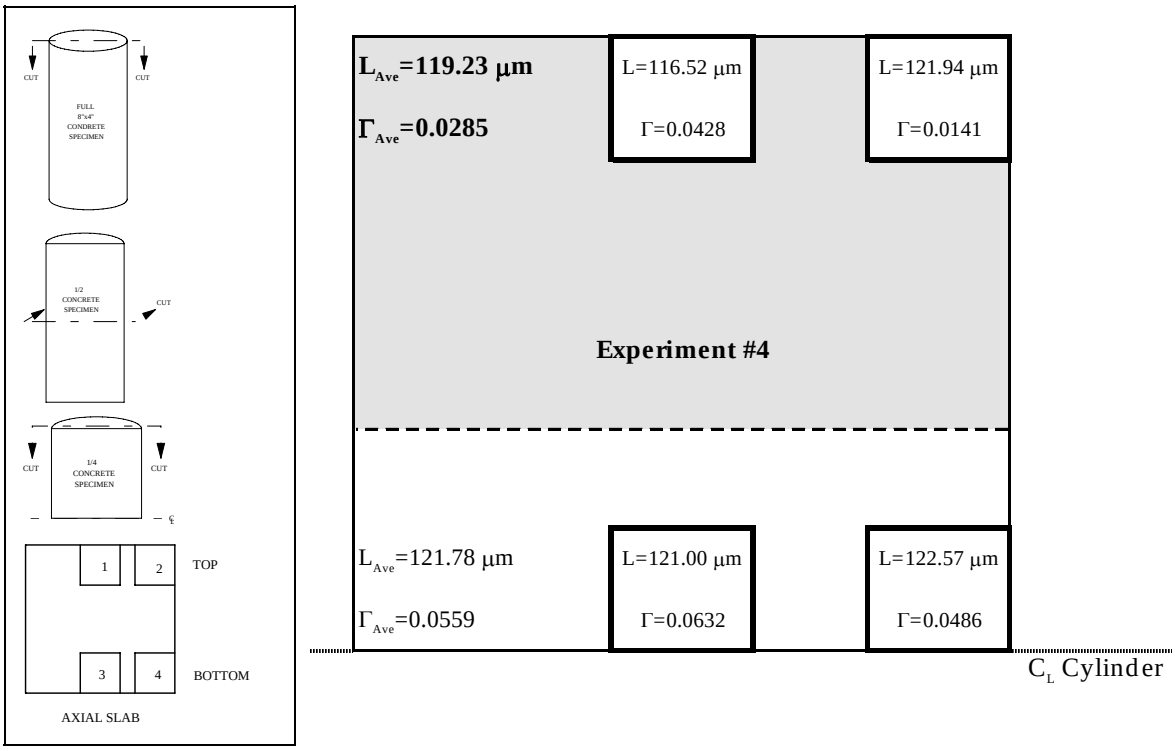

Figure 4.19 Diagrammatic representation of crack length and crack density at confined and unconfined portions of Experiment #4

Another way of assessing the crack density is by counting the number of microcracks per unit of observation area (see Table 4.1). Pore spaces were not counted as microcracks. Figures 4.20 and 4.21 show that the number of cracks is strongly influenced by confining condition for both types of concrete.

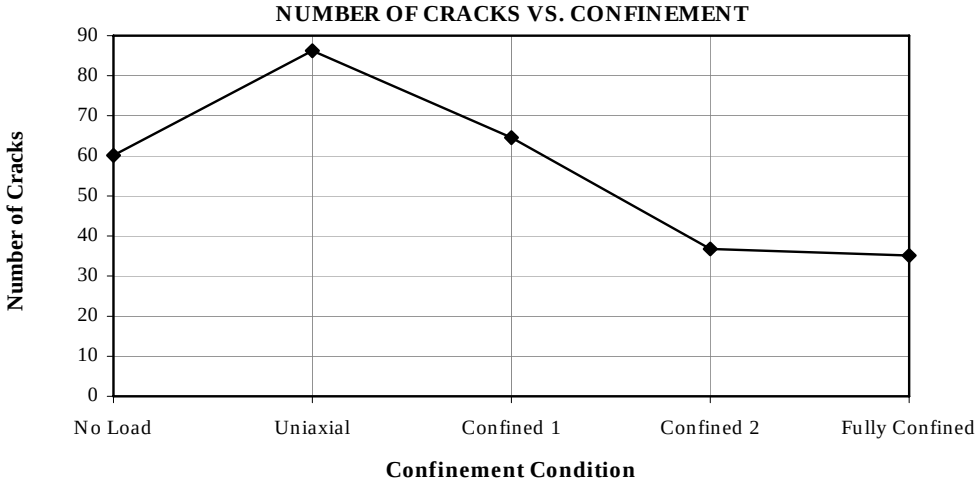

Figure 4.20 Number of cracks as a function of confinement for normal-strength concrete

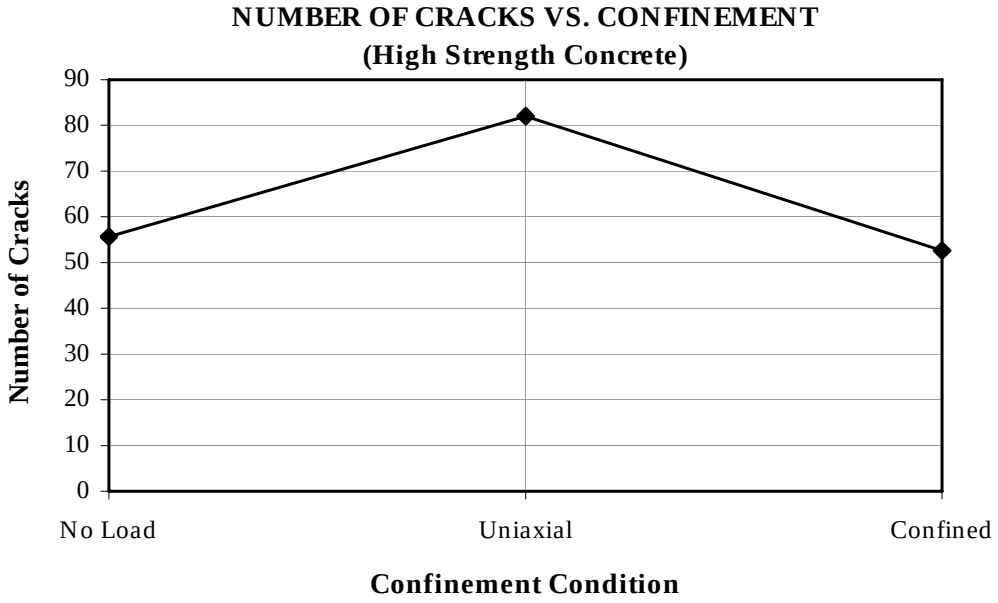

Figure 4.21 Number of cracks as a function of confinement for high-strength concrete

Crack density can also be measured in terms of percent cracked area (see Table 4.2). Figures 4.22 and 4.23 are the plots of percent cracked area as a function of confinement. Again, percent cracked areas decrease as the confinement increases, for both normal and high-strength concrete specimens.

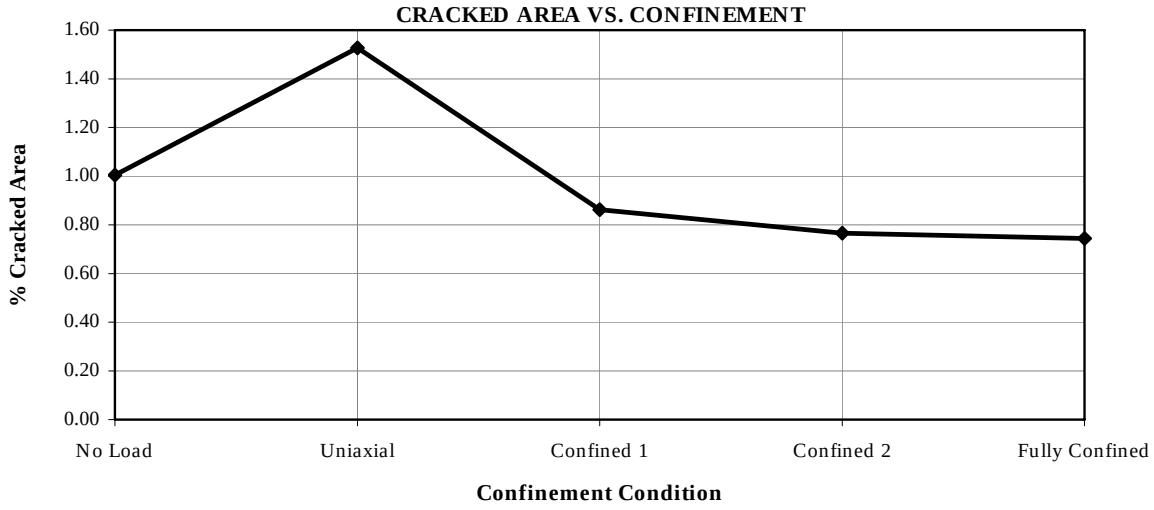

Figure 4.22 Percent cracked area as a function of confinement for normal-strength concrete

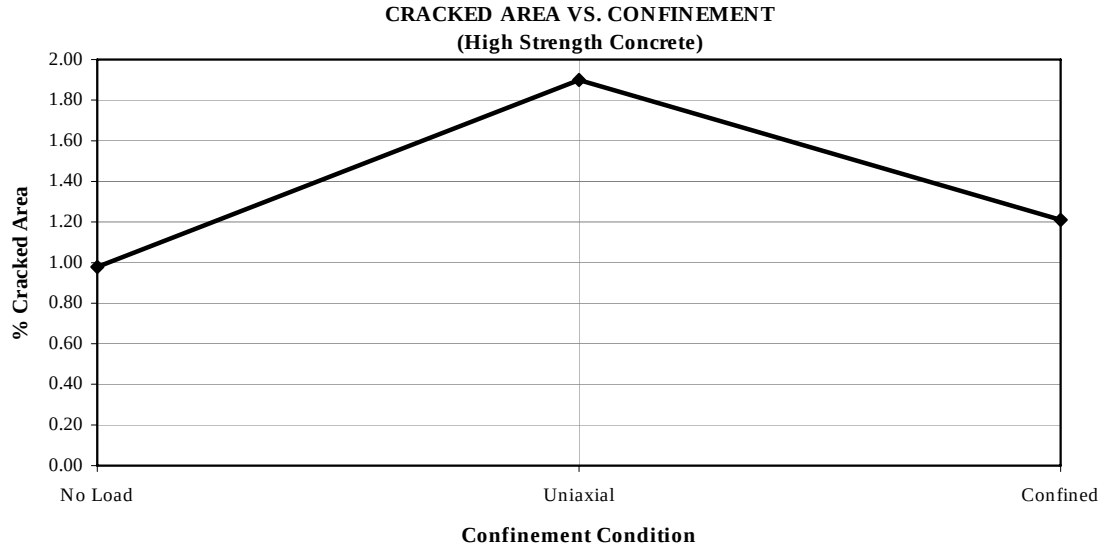

Figure 4.23 Percent cracked area as a function of confinement for high-strength concrete

The influence of confining stress on microcrack density was described by Kranz (1983) as follows. Microcracks are generated by local tensile stresses, which depend on the geometry of pores and aggregates, and material heterogeneity, as well as magnitude and direction of applied stresses. With increasing confining stress, an increasing hydrostatic stress is applied to the concrete; as a result, the local tensile stress which is responsible for the generation of microcracks is reduced. The superposition of hydrostatic pressure upon an existing deviatoric stress field is likely to decrease the range and magnitude of deviatoric stresses concentrated near crack tips, as well as increase frictional resistance to shear between crack surfaces in contact. For extensile cracks, this increases the energy of stress requirements for propagation and thereby makes crack interaction less probable. This most probably explains the decreasing microcrack density when confining stress is introduced.

The stereological measurement of the surface-to-volume ratio, S_V (S/V), was determined from the basic equation for obtaining the total crack surface area per unit of volume. Plots of S_V as a function of confinement are presented in Figures 4.24 and 4.25 for normal-strength and high-strength concrete specimens, respectively.

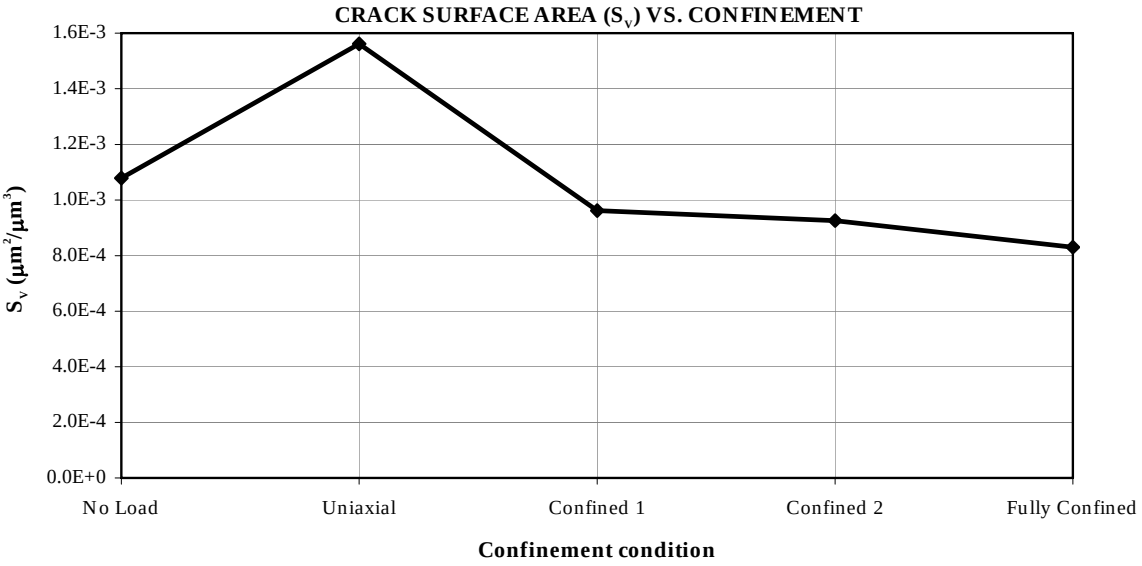

Figure 4.24 Crack surface area (S_V) as a function of confinement condition for normal-strength concrete

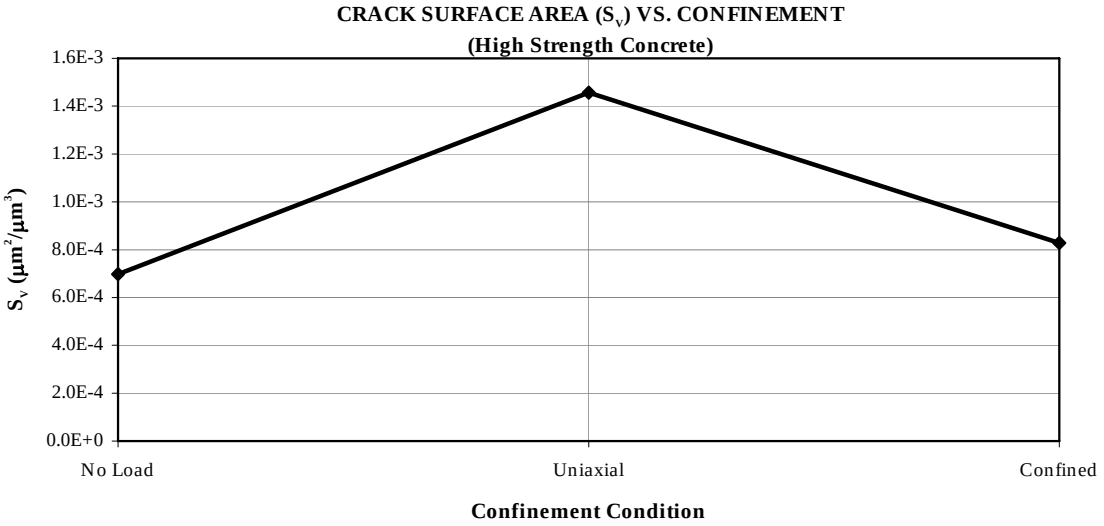

Figure 4.25 Crack surface area (S_V) as a function of confinement condition for high-strength concrete

Crack surface area, S_V, decreases as the confining stresses increases in both normal and high-strength concrete cases.

4.5 MICROCRACK LENGTH DISTRIBUTION

The average length distribution of the microcracks strongly depends on the confining stress. In the specimen subjected to uniaxial compression, most of the microcracks propagated to a certain length and stopped. When confining stress was introduced, the average length of the microcracks decreased, as indicated in Figures 4.26 and 4.27. With increasing confining stress, the average length of microcracks decreased. Specimen #5, which was fully confined, had the lowest crack length. In the partially confined specimens (Experiments #3 and #4), the influence of confinement of the crack length is illustrated in Figures 4.18 and 4.19, which show clearly that the average length distribution of microcracks is strongly dependent on the confining stress.

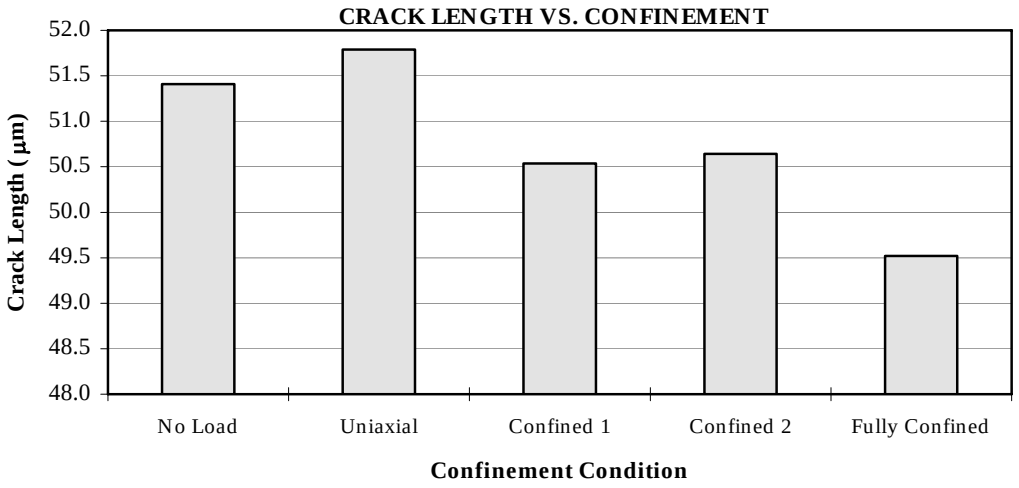

Figure 4.26 Crack length as a function of confinement condition for normal-strength concrete specimens

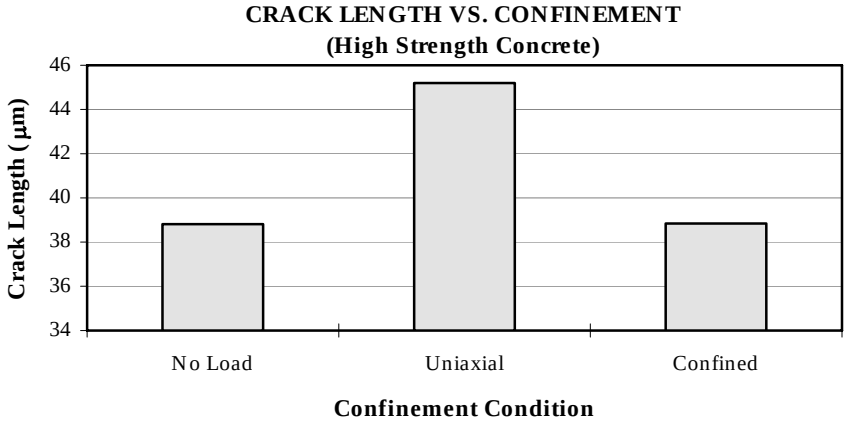

Figure 4.27 Crack length as a function of confinement condition For high-strength concrete specimens

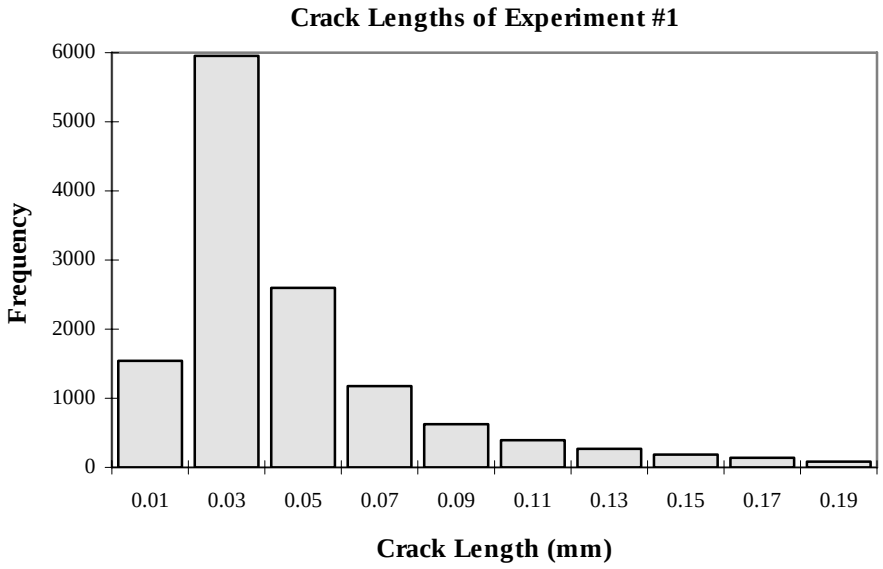

Figure 4.28 Histogram of microcrack length distributions for the no-load experiment of the normal-strength concrete

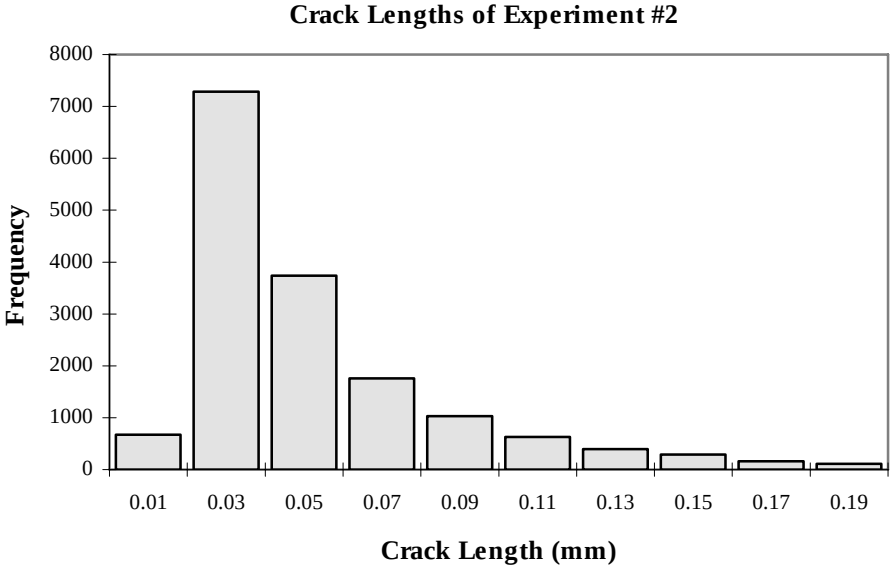

Figure 4.29 Histogram of microcrack length distributions for the uniaxial experiment of the normal-strength concrete

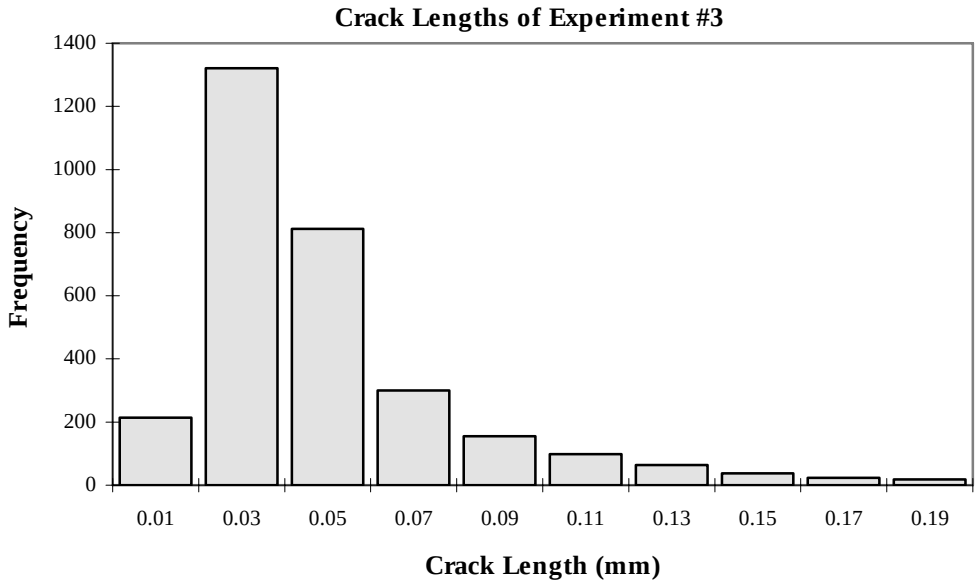

Figure 4.30 Histogram of microcrack length distributions for the partially confined (1) experiment of the normal-strength concrete

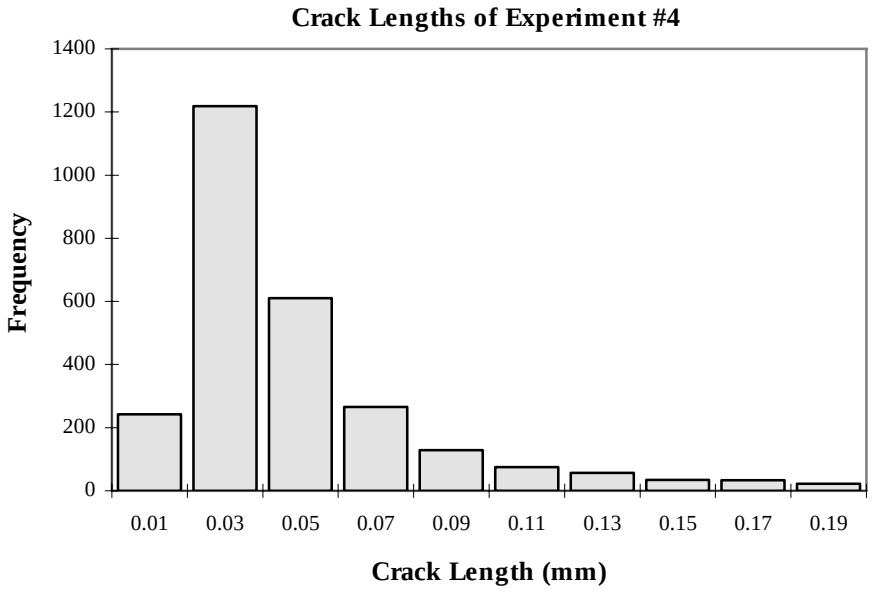

Figure 4.31 Histogram of microcrack length distributions for the partially confined (2) experiment of the normal-strength concrete

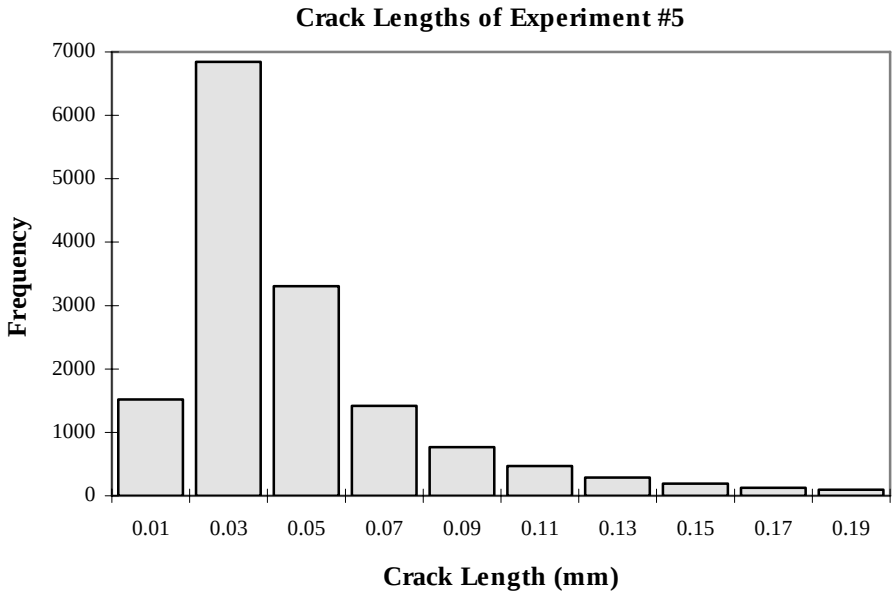

Figure 4.32 Histogram of microcrack length distributions for the fully confined experiment of the normal-strength concrete

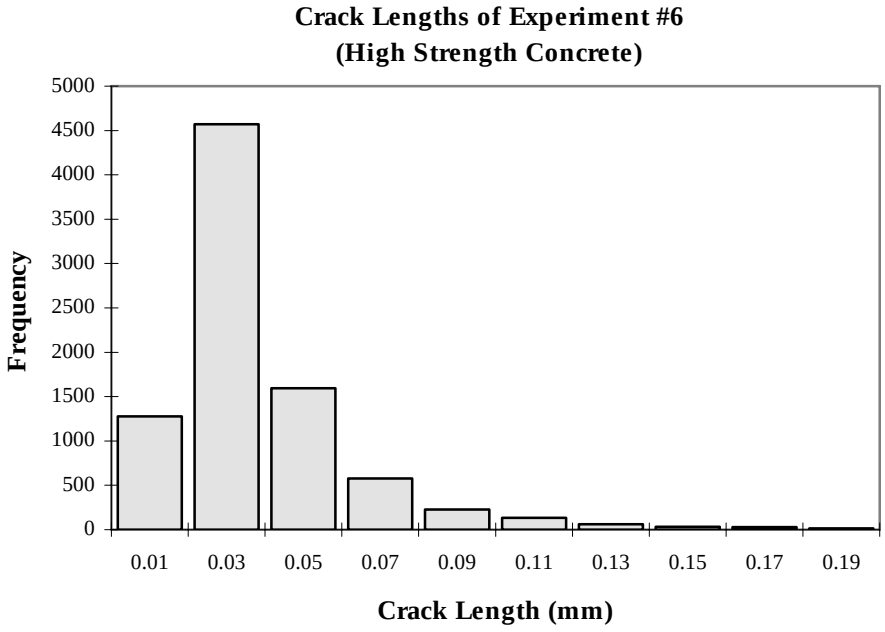

Figure 4.33 Histogram of microcrack length distributions for the no-load experiment of the high-strength concrete

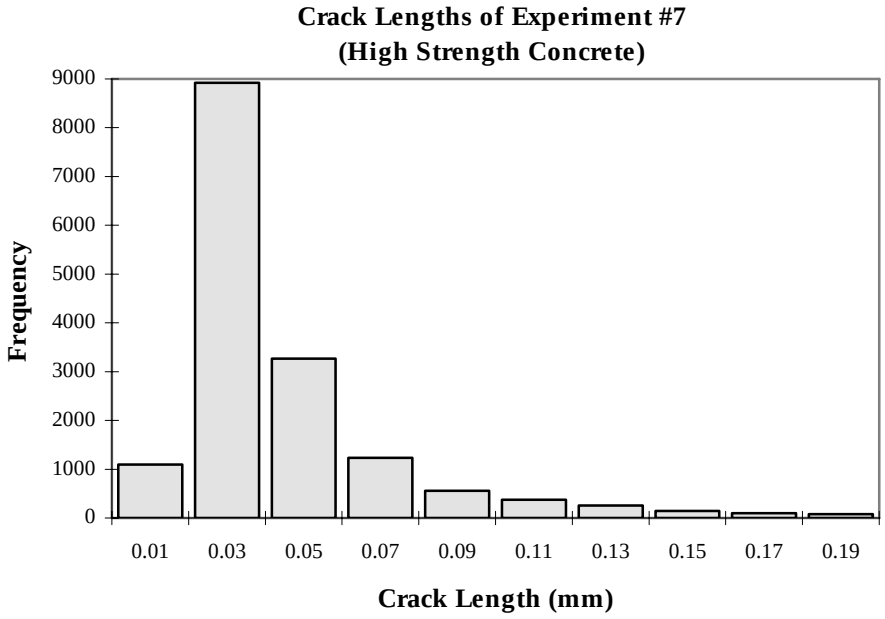

Figure 4.34 Histogram of microcrack length distributions for the uniaxial experiment of the high-strength concrete

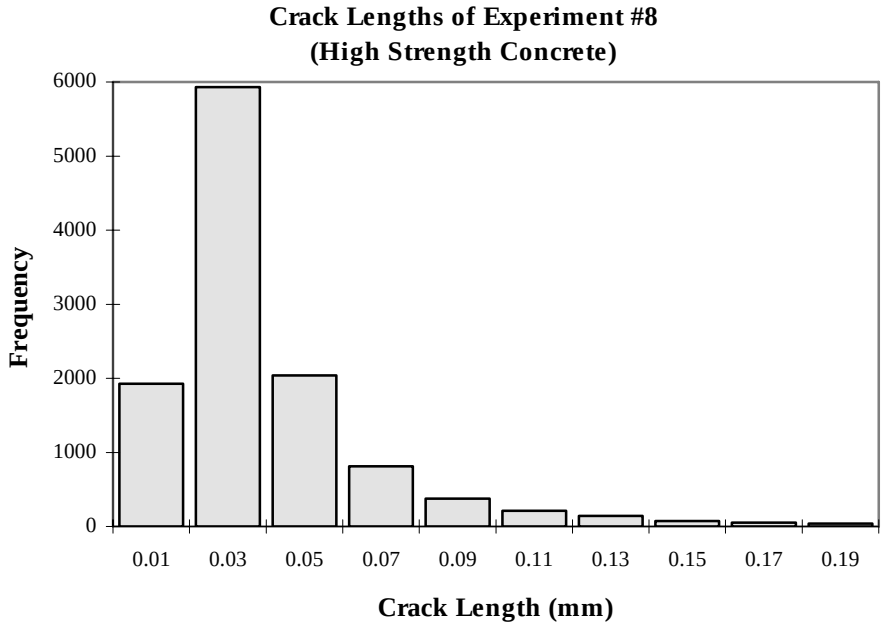

Figure 4.35 Histogram of microcrack length distributions for the partially confined experiment of the high-strength concrete

With increasing confining stress, both the average lengths of microcracks and the ratio of their standard deviation to average length, known as the coefficient of variation (COV), decreased. Figures 4.28 through 4.35 show the crack length histograms of five normal-strength and three high-strength concrete specimens.

Table 4.4 Tabulates the crack length, standard deviation, and the coefficient of variation for all the experiments.

Table 4.4 Coefficient of variation of crack length

Conc. Type	Experiment Type	Avg. Crack Length (mm)	Standard Deviation	Coef. of Variation
Normal Strength Concrete	**No Load**	0.05086	0.0506	0.99
	Uniaxial	0.05552	0.0454	0.82
	Confined 1	0.05248	0.0430	0.82
	Confined 2	0.05149	0.0413	0.80
	Fully Confined	0.04959	0.0390	0.79
High Strength Concrete	**No Load**	0.03922	0.0303	0.77
	Uniaxial	0.04996	0.0589	1.18
	Confined	0.04200	0.0387	0.92

Figures 4.36 and 4.37 are the plot of the coefficient of variation as a function confining condition for normal-strength and high-strength concrete specimens.

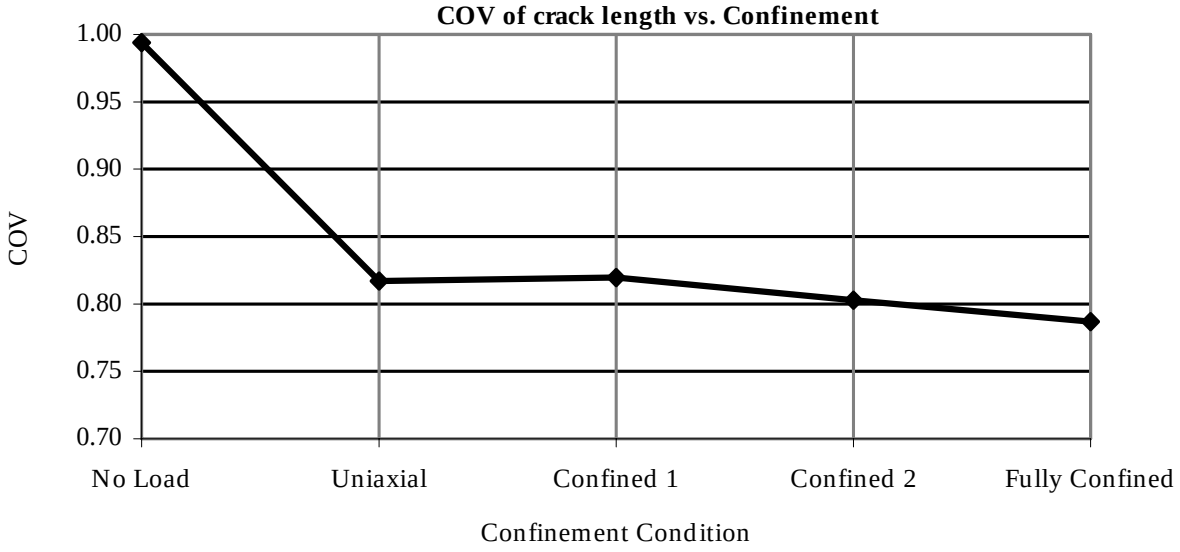

Figure 4.36 COV of crack length as a function of confinement for normal-strength concrete

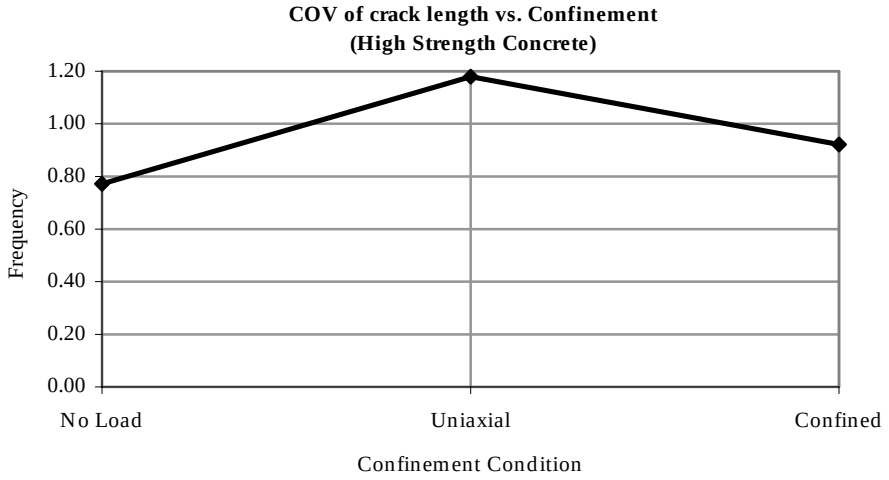

Figure 4.37 COV of crack length as a function of confinement for high-strength concrete

Table 4.4 and Figures 4.36 and 4.38 indicate that with increasing confining stress, the average lengths and the coefficient of variation of crack lengths (the ratio of standard deviation of microcrack lengths to average length of microcracks) decrease.

The stress intensity factor is a fundamental quantity that governs the stress field near the crack tip. The propagation of microcracks is controlled by the stress intensity factor at the microcrack tips, resulting from both local tensions, which generate the microcracks, and the overall stress field. The confining stress, which is orthogonal to the direction of maximum compression, adds a negative stress intensity factor, which stops the propagation of the extensile microcracks (Zheng 1989) (Figure 4.38).

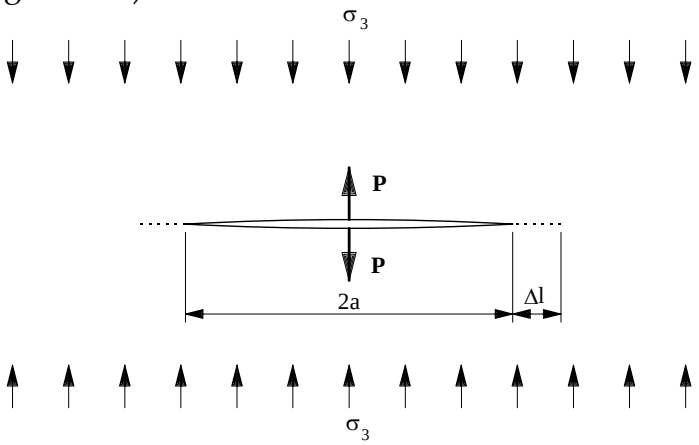

Figure 4.38 Stress intensity factors due to local tension P and confining stress, σ_3 ($K_I = P/\sqrt{\pi l}$ and $K_I = \sigma_3\sqrt{\pi l}$)

This negative stress intensity factor increases (in the negative sense) in proportion to the increase in confining stress. As a result, crack lengths are reduced by an increase in confining stress. Using a centrally loaded crack model from linear elastic fracture mechanics, a simple equation for the crack length under confining stress, relative to an unconfined crack, can be expressed as follows (Zheng 1989):

$$L=\frac{2}{\pi}\left(\frac{\sigma_t \beta}{K_{IC}}\right)^2 \tag{4.3}$$

for σ_r=0, and

$$L=\frac{2}{\pi}\left(\frac{\sqrt{K_{IC}{}^2-4\beta\sigma_r\sigma_t}-K_{IC}}{2\sigma_r}\right)^2 \tag{4.4}$$

for $\sigma_r \neq 0$

where: L = microcrack length

K_{IC} = fracture toughness of concrete

σ_r = confining stress

σ_t = local tensile stress responsible for the microcrack generation

β = efficient depending on the geometry and boundary conditions of the microcracks.

Because the microcracks are produced by local tensile stresses, the driving forces from the local tensile stresses decrease as the microcrack length increases. On the other hand, the negative driving forces applied by the confining stress increase as the microcrack length increases. The combined effect of these two arguments is a great reduction in microcrack length under high confining stress.

Based on stereological analysis, L_A, the length of line per unit area also decreases with increasing confining stresses. Figures 4.39 and 4.40 show the relationship between L_A and confinement condition for normal and high-strength concrete.

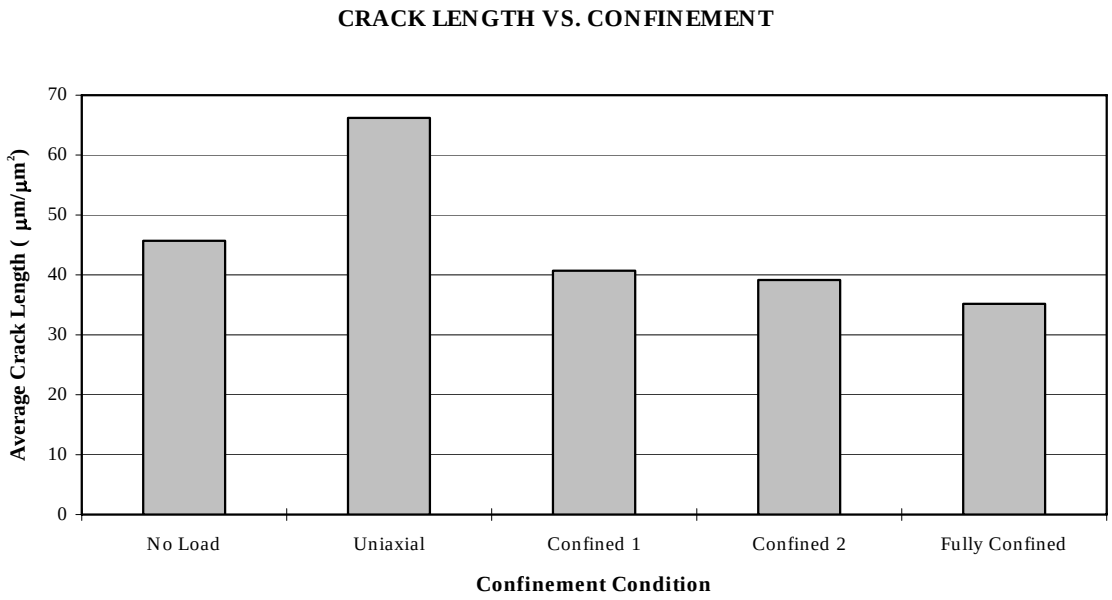

Figure 4.39 Stereological measurement of crack length as a function of confinement condition for normal-strength concrete specimens

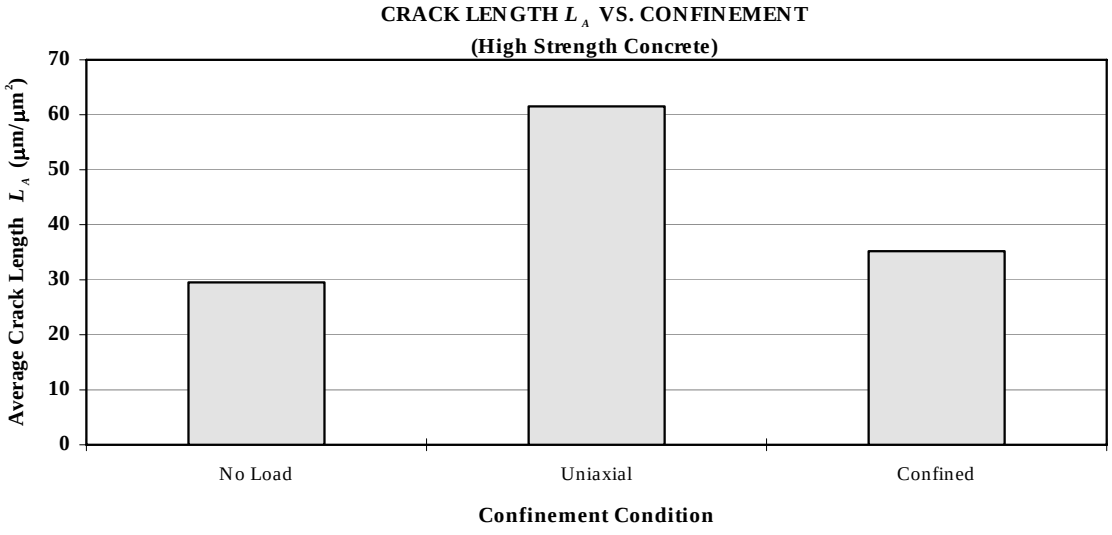

Figure 4.40 Stereological measurement of crack length as a function of confinement condition for high-strength concrete specimens

4.6 MICROCRACK BRANCHING

Cracks with frequent branching are often observed in the fracture process of brittle and quasi-brittle materials such as ceramics and concrete. The crack branching patterns of materials are very complex and irregular; however, quantitative analysis of branching patterns could reveal some important information about the stress applied during crack propagation, as well as material characteristics such as surface energy and the elastic constant (Nakasa and Nakatsuka 1991, 1994). Fractal analysis has also been applied to complex branching patterns (Mandelbrot 1977).

For crack branching analysis, a computer program has been developed to measure the number of 3-way and 4-way crack-branching nodes similar to the ones shown in Figure 4.41 (see Appendix B).

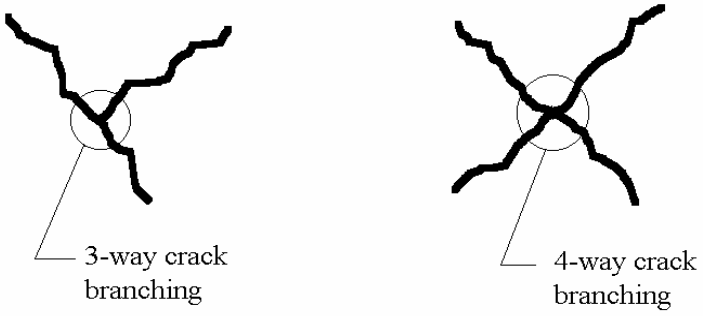

Figure 4.41 3-way and 4-way crack branching nodes

Figures 4.42 and 4.43 show that as the confining stress increases, the number of crack branching nodes decreases. This is expected by the fact that since the propagation of microcracks is controlled by the stress intensity factor at the microcrack tips, as the confining stress increases, the negative stress intensity factor imposed by confinement increases proportionately. This limits the energy required for cracks to grow and branch off. The amount of branching in the high-strength concrete is considerably less than the number of cracks in the normal-strength concrete. This can be attributed to the fact that high-strength concrete is much more brittle than normal-strength concrete. As a result, when

fracture occurs in high-strength concrete, the crack propagation is associated with less branching.

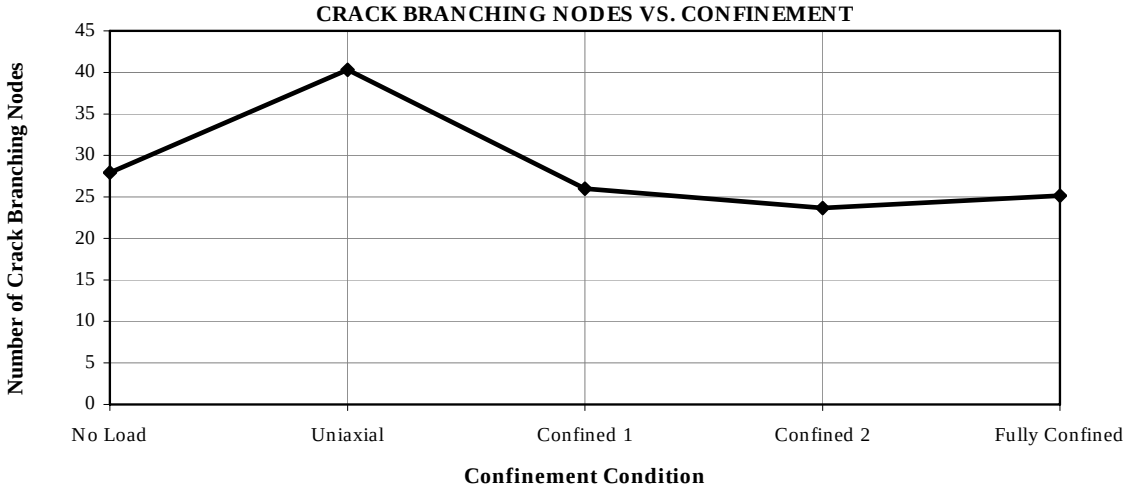

Figure 4.42 Crack-branching nodes as a function of confinement for normal-strength concrete

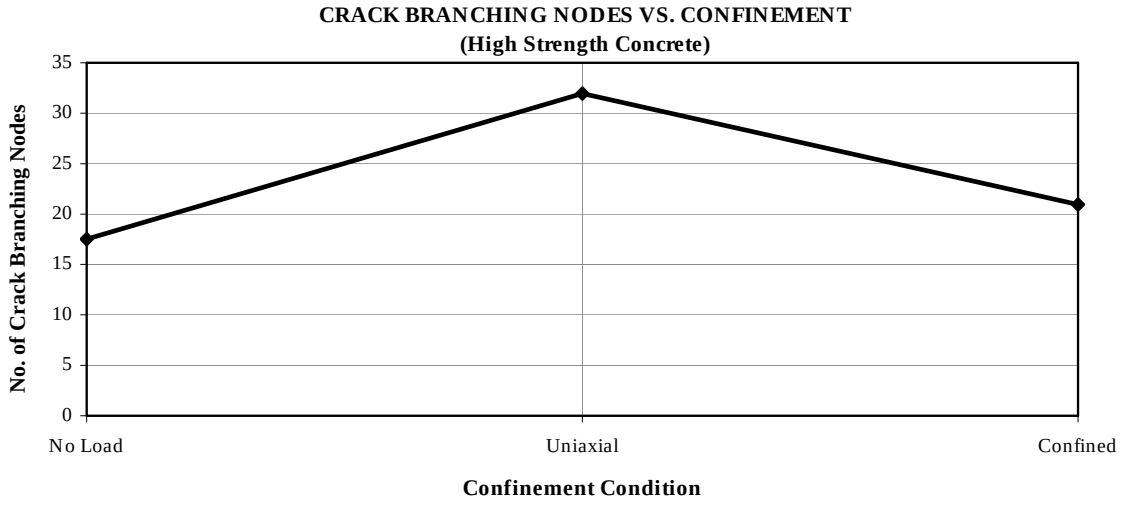

Figure 4.43 Crack-branching nodes as a function of confinement for high-strength concrete

4.7 INTERFACIAL CRACKS

Investigations have shown that very fine cracks at the interface between coarse aggregate and cement paste exist even prior to application of the load on concrete (Hsu et al. 1963). The transition zone, which is the region between hydrated cement paste and coarse aggregate, is a thin shell with a thickness of 10 to 50 μm, and is considered to be weaker than the two main components of concrete: cement paste and aggregate. Crack initiation and propagation are the dominant mechanisms responsible for the nonlinear response of concrete subjected to uniaxial compressive loading. Cracks may initiate in the matrix, aggregates, or in the matrix-aggregate interface.

Interfacial cracks remain stable up to about 30 percent or more of the ultimate strength and then begin to increase in length, width, and number. The overall stress under which they develop is sensitive to the water/cement ratio of the paste. This is the stage of slow crack propagation. At 70 to 90 percent of the ultimate strength, cracks open through the cement paste and bridge the interfacial cracks and the continuous crack pattern is formed (Neville 1981). Because of slow chemical interaction between the cement paste and aggregate, at later ages the transition zone strength improves more than the bulk cement paste strength.

Studies conducted using microscopic analysis (Hsu et al. 1963; Shah and Chandra 1970; Shah and Sankar 1987) have revealed that cracks frequently initiate at the interface and then propagate into the matrix where mortar cracks join to form a continuous crack path prior to ultimate load. In order to analyze the phenomenon of interfacial cracking, an attempt has been made in this section to characterize these cracks. Using advanced computerized imaging, a computer program has been developed to identify interfacial cracks and distinguish them from matrix cracks (see Appendix B). Figure 4.44 shows the flow chart for the computer program.

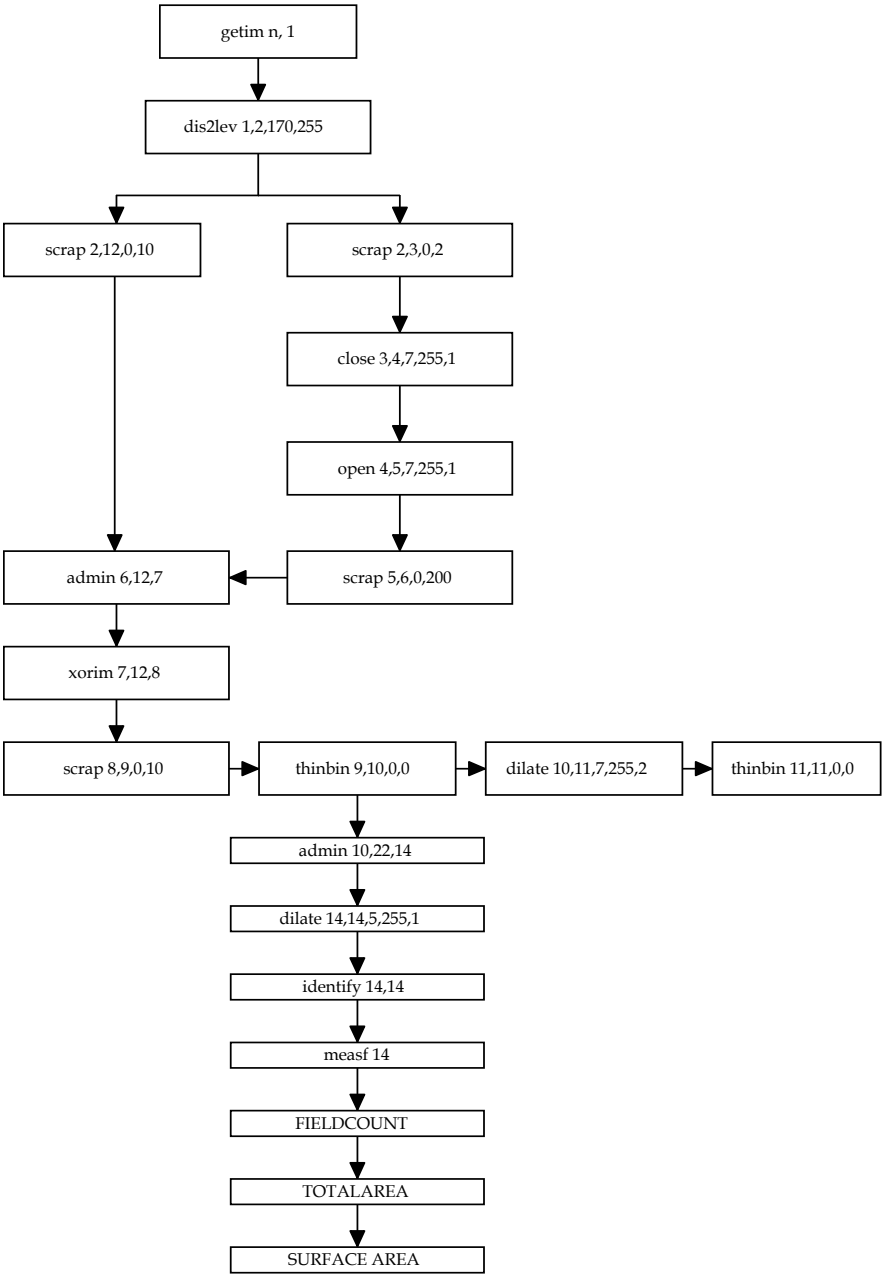

Figure 4.44 The flow chart for interfacial crack identification computer program

The step-by-step procedure for the computer program is outlined below. Figure 4.45 is a SEM image of a concrete specimen which was subjected to a uniaxial loading.

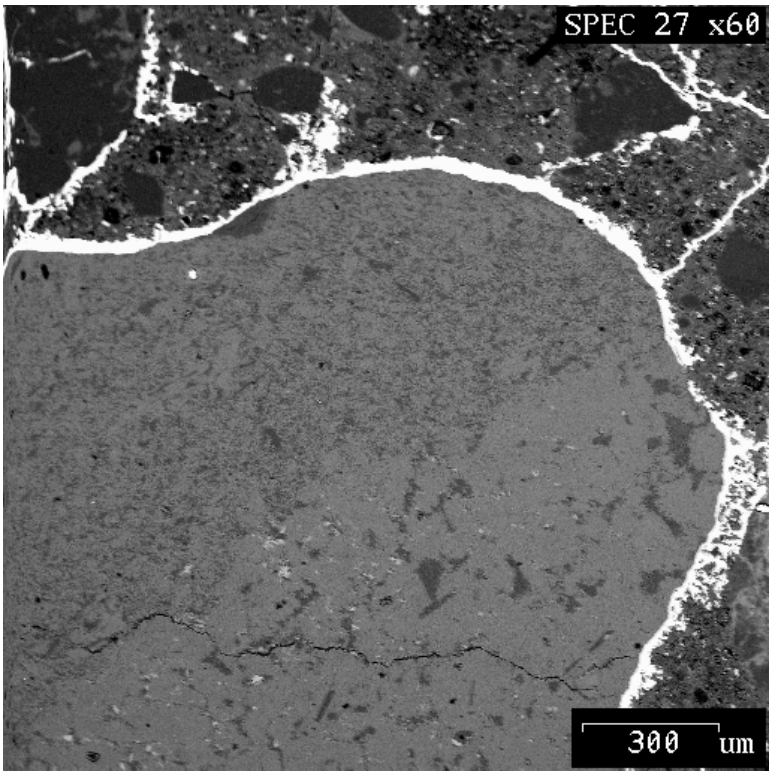

Figure 4.45 Interfacial crack in the normal concrete specimen subjected to uniaxial loading

Using the same criteria outlined in Section 3.4.4 of Chapter 3 for Wood's metal identification, a binary image showing the untreated crack network is produced. In order to eliminate objects on the basis of their area in pixel units, the *scrap* command is invoked for two different *areahigh* values of 2 and 10, indicating the upper limit for the area range (in pixels). Figures 4.46 and 4.47 represent the scraped images of Figure 4.45 with the areahighs of 10 and 2, respectively.

The *close* command first dilates objects in the binary image using a structuring element, defined by shape, i.e. an octagon; it then erodes them, using the same structuring element. This procedure merges adjacent objects. The close command is used on Figure 4.47, which produces Figure 4.48.

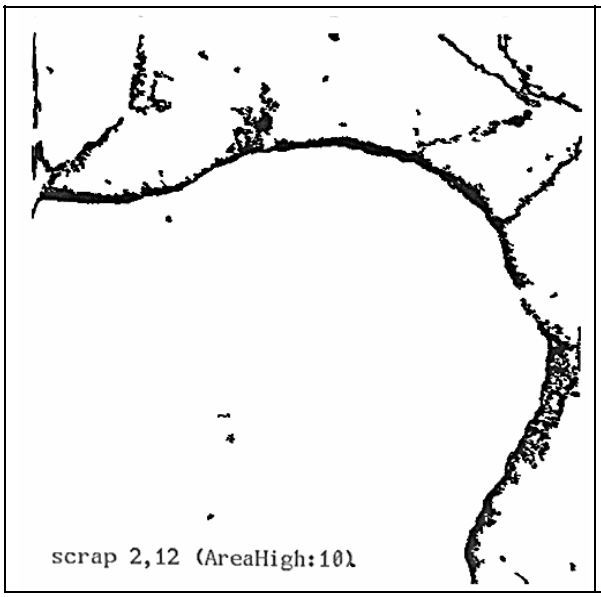

Figure 4.46 Scrap with the higher upper limit for the area range

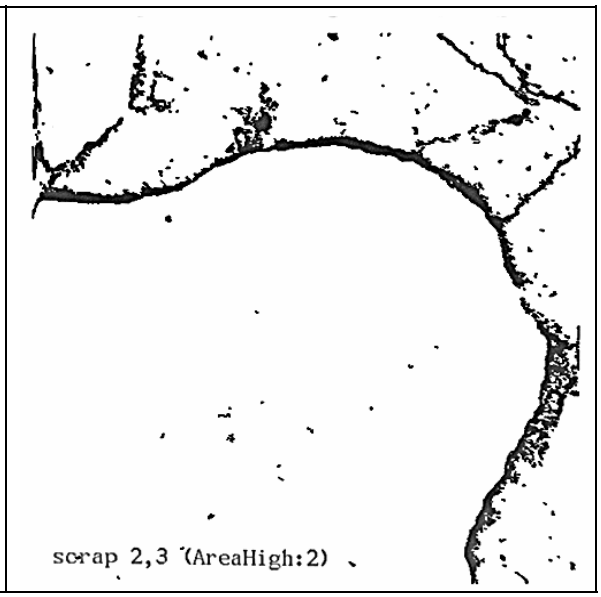

Figure 4.47 Scrap with the lower upper limit for the area range

The *open* command initially erodes the object in a binary image by means of a structuring element defined by shape, similar to the one used in the *close* command; it then dilates it by means of the same structuring element. This procedure eliminates small objects without strongly affecting larger ones. The open command is used on the image in Figure 4.48 to produce Figure 4.49.

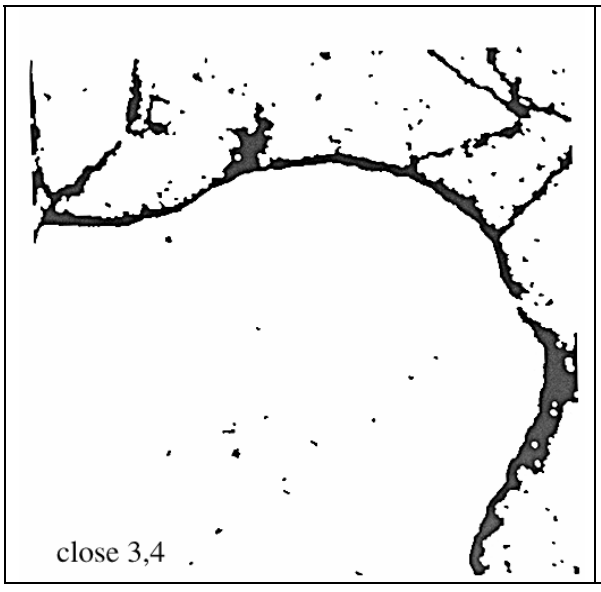

Figure 4.48 Close the image in Figure 4.47

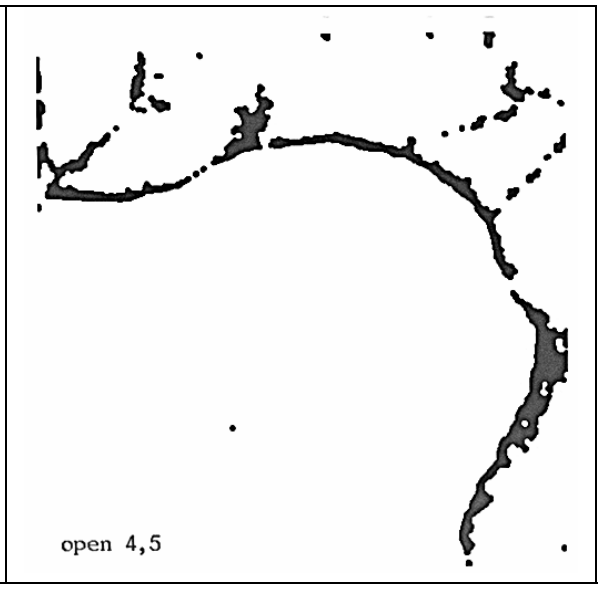

Figure 4.49 Open the image in Figure 4.48

Figure 4.50 Scrap the image in Figure 4.49

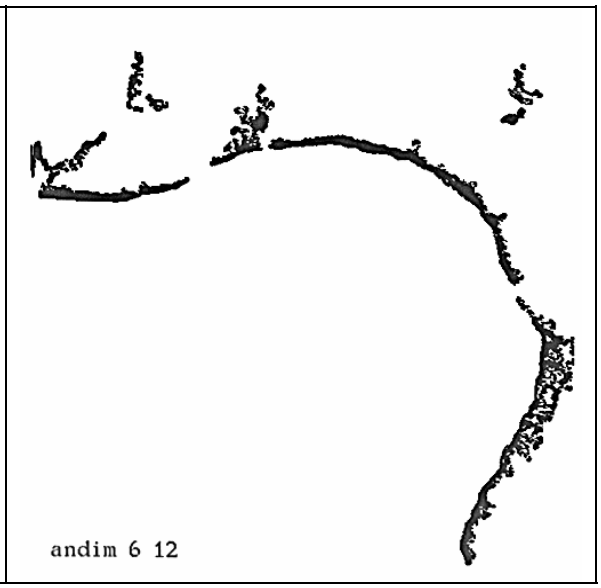

Figure 4.51 Correlate every pixel which is both in Figure 4.46 and 4.50

The loose objects in Figure 4.49 are scrapped and Figure 4.50 is produced. At this point every pixel which is both in Figures 4.50 and 4.46 is correlated, which results in the image shown in Figure 4.51. This task is achieved by invoking the *andim* command.

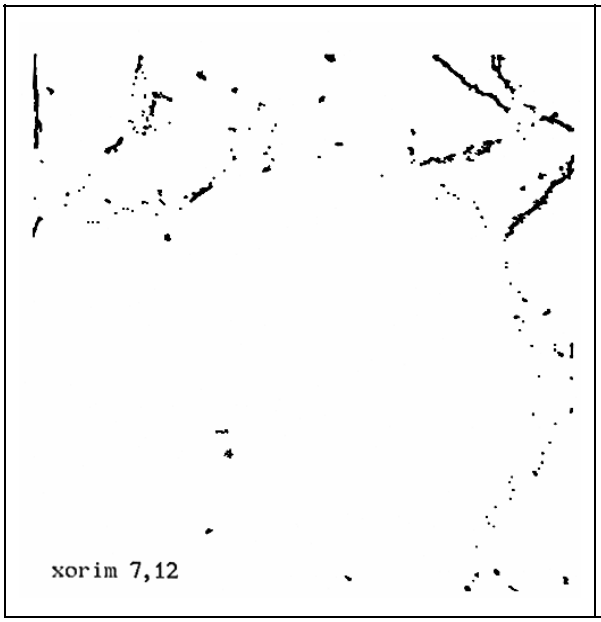

Figure 4.52 Correlating every pixel that is either in Figure 4.46 or 4.49 but not common to them

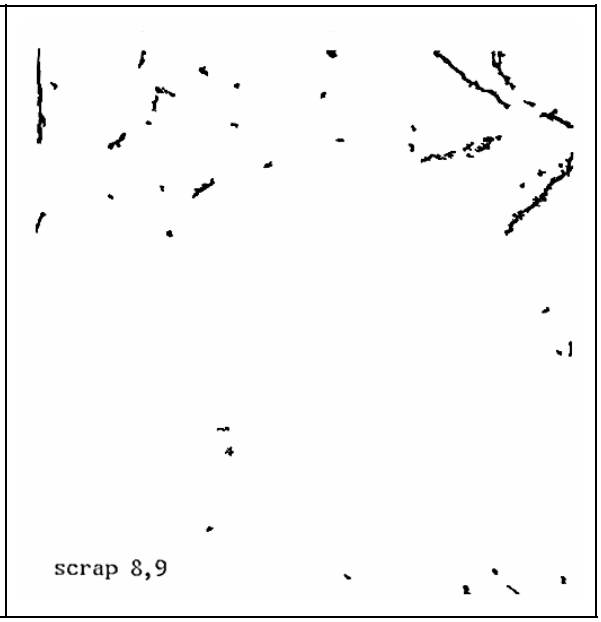

Figure 4.53 Scrap the image in Figure 4.52

Figure 4.52 is subjected to the *xorim* command. *Xorim* (exclusive or) correlates every pixel that is either in Figure 4.51 or 4.46 but not common to Figure 4.51 and 4.46, and the result is outputted in Figure 4.52. The *scrap* command is applied to the image in Figure 4.52 to produce Figure 4.53.

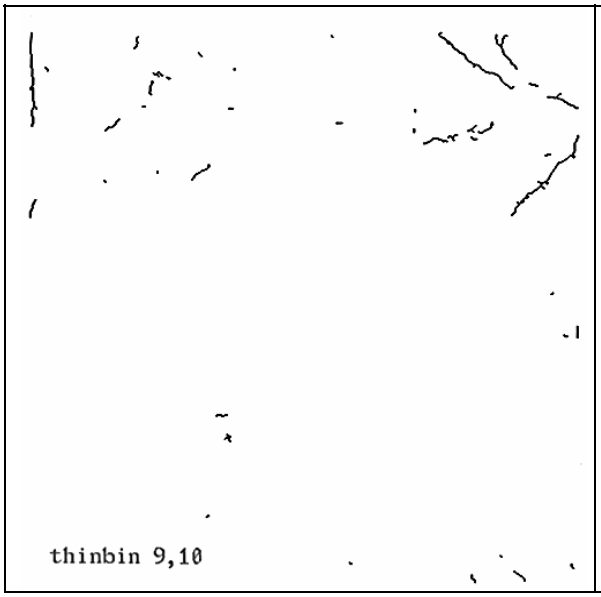

Figure 4.54 Scrap Figure 4.52

Figure 4.55 Crack smoothing of the image in Figure 4.54

Figure 4.53 was subjected to binary thinning and Figure 4.54 is the result. The crack network in Figure 4.54 is dilated and then thinned again to produce Figure 4.55, which is an image of the cracks after they have been smoothed. Figures 4.54 and 4.55 represent the cracks in the concrete matrix, discounting the interfacial cracks. Stereological measurements can be performed on the image in Figure 4.54 to investigate the crack behavior in the cement paste.

Measurements were performed on the total area of the cracks and the area of the interfacial cracks in the SEM images, and the percentage of interfacial cracks obtained is presented in Table 4.5.

Figure 4.56 shows the percentage of interfacial microcracks as a function of the confining stress for normal-strength concrete. As shown, there is a sharp reduction in the amount of interfacial microcracks as the confining stress

increases. The greatest reduction occurred when the concrete specimen was fully confined.

Table 4.5 Percentage of interfacial microcracks

Concrete Type	EXPERIMENT	AREA	I.F. AREA	% AREA
Normal Strength Concrete	No-Load	30569	8510	27.8%
	Uniaxial	68079	17109	25.1%
	Confined 1	73781	17549	23.8%
	Confined 2	47910	9954	20.8%
	Fully Confined	40728	3006	7.4%
High Strength Concrete	No-Load	5885	450	7.6%
	Uniaxial	16283	1103	6.8%
	Confined	3041	204	6.7%

Figure 4.57 shows the percentage of interfacial cracks as a function of confinement for the high-strength concrete specimen. As in normal-strength concrete, interfacial cracks were heavily influenced by the confining stress.

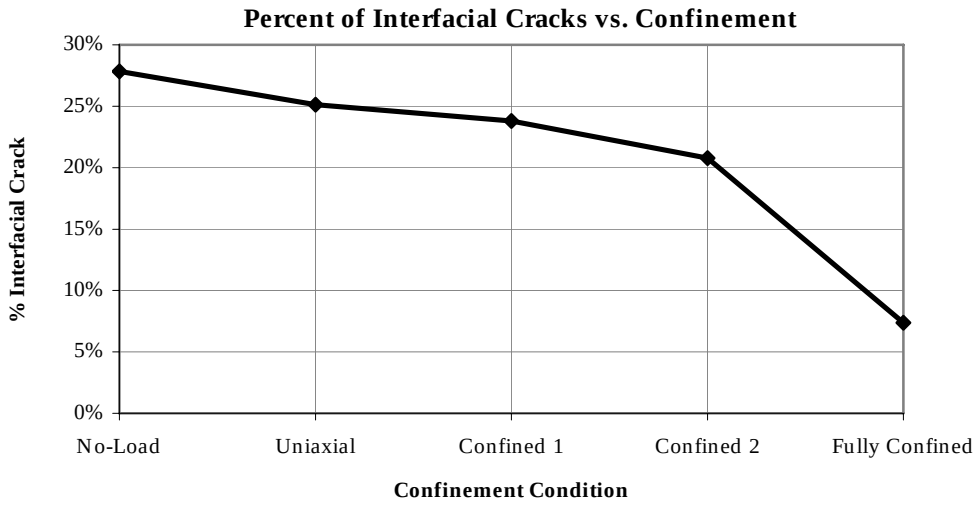

Figure 4.56 Effect of confinement on interfacial microcracks of normal-strength concrete

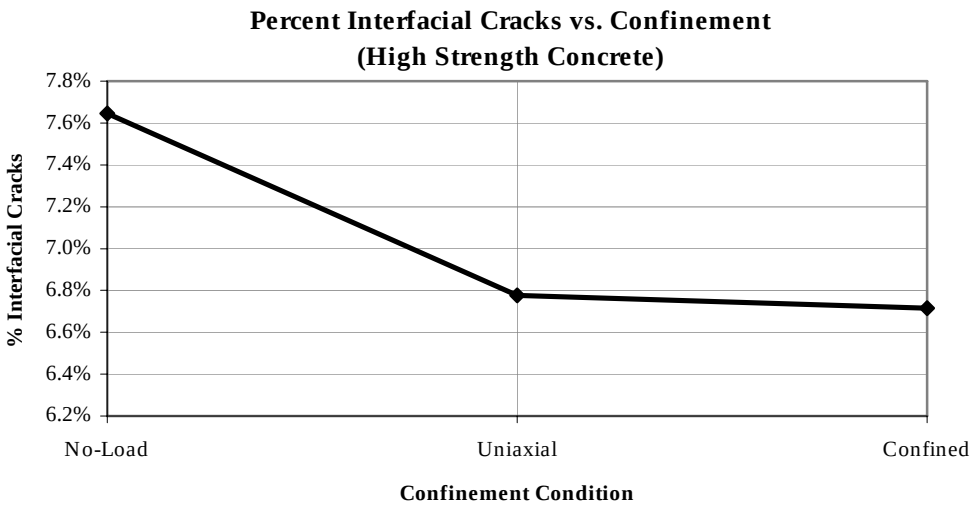

Figure 4.57 Effect of confinement on the interfacial microcracks of high-strength concrete